



HAL
open science

A novel laser-based method to measure the adsorption energy on carbonaceous surfaces

D. Duca, C. Pirim, M. Vojkovic, Y. Carpentier, A. Faccinetto, M. Ziskind, C. Preda, C. Focsa

► To cite this version:

D. Duca, C. Pirim, M. Vojkovic, Y. Carpentier, A. Faccinetto, et al.. A novel laser-based method to measure the adsorption energy on carbonaceous surfaces. *Carbon*, 2020, 173, pp.540-556. 10.1016/j.carbon.2020.10.064 . hal-03418708

HAL Id: hal-03418708

<https://hal.science/hal-03418708v1>

Submitted on 8 Nov 2021

HAL is a multi-disciplinary open access archive for the deposit and dissemination of scientific research documents, whether they are published or not. The documents may come from teaching and research institutions in France or abroad, or from public or private research centers.

L'archive ouverte pluridisciplinaire **HAL**, est destinée au dépôt et à la diffusion de documents scientifiques de niveau recherche, publiés ou non, émanant des établissements d'enseignement et de recherche français ou étrangers, des laboratoires publics ou privés.

A novel laser-based method to measure the adsorption energy on carbonaceous surfaces

D. Duca^a, C. Pirim^a, M. Vojkovic^a, Y. Carpentier^a, A. Faccinetto^b, M. Ziskind^a, C. Preda^c, C. Focsa^{a,*}

^aUniv. Lille, CNRS, UMR 8523 – PhLAM – Laboratoire de Physique des Lasers Atomes et Molécules, F-59000 Lille, France

^bUniv. Lille, CNRS, UMR 8522 – PC2A – Physicochimie des Processus de Combustion et de l’Atmosphère, F-59000 Lille, France

^cUniv. Lille, CNRS, UMR 8524 – Laboratoire de Mathématiques Paul Painlevé, F-59000 Lille, France

Abstract

The reactivity of carbonaceous surfaces bears a fundamental role in various fields, from atmospheric chemistry and catalysis to graphene and nanoparticles. This reactivity is mainly driven by the surface chemical composition and by the strength of the interaction between the adsorbates and the surface (physi-/chemisorption). While the surface composition of complex natural samples can be well characterized, adsorption energies (ergo, adsorption processes) of the corresponding adsorbate/adsorbent systems are often overlooked. We propose a novel laser-based method for measuring the adsorption energy of chemical species on various carbonaceous surfaces. The proof of concept of this original method has first been demonstrated by deriving adsorption energies of various systems consisting of polycyclic aromatic hydrocarbons and activated carbon. The great potential of this fast, spatially resolved, and surface-sensitive method, which can also act as a defect density probe at the mesoscale, has been further demonstrated through the study of systems of increasing complexity.

Keywords: Carbonaceous surfaces, Adsorption energy, Laser-induced thermal desorption, Mass spectrometry, Bayesian statistics

1. Introduction

Carbonaceous materials are used in a wide range of applications including aerospace and defense, automotive, energy, construction, electronics, and sports. Their superior properties including excellent stiffness, high tensile strength, low thermal expansion, and good temperature tolerance [1, 2], make them versatile materials that can be shaped into various forms depending upon the use intended (*e.g.* carbon fibers, carbon nanotubes, graphene). Carbon-based materials can also be turned into metal-free catalysts and serve as a promising alternative to transform sustainable biomass into renewable energy systems [3].

Due to their excellent adsorption capacities, carbonaceous materials are widely employed as filtration media. Carbon nanotubes (CNT) show great

potential at revolutionizing water and gas treatment technologies [4] as they provide much higher surface areas, adsorption capacities, and faster kinetics than activated carbon, the currently prevailing filtration agent. The utility of the adsorptive fixation of organics in the gas and liquid phases for treating wastewaters and emission gasses is already showcased for a number of harmful compounds [5–8]. Another considerable advantage of carbon nanostructures is that their properties can be tailored to target certain chemical species (*e.g.* toxins, heavy metal ions) [4, 9, 10].

For carbonaceous materials, the downside of exhibiting high adsorptive capacities is that they will act as surface carriers. This can lead to adsorbed toxic species undergoing long-range transport in the atmosphere. This effect is commonly observed with combustion generated aerosols (soot), which consist of a carbonaceous matrix often coated with a plethora of organic species [11–13], many of them exhibiting a proven carcinogenic potential [14–16].

*Corresponding author. Tel.: +33 675 482 049

Email address: cristian.focsa@univ-lille.fr (C. Focsa)

39 This makes the impact of combustion generated
40 particles on human health considerably greater, es-
41 pecially since their inhalation can result in health
42 problems beyond the lungs [17]. In fact, the pres-
43 ence of combustion derived nanoparticles has been
44 detected in the frontal cortex of autopsy brain sam-
45 ples [18], urine of healthy children [19], and even in
46 the fetal side of the placenta [20]. If transported
47 to the fetus, these particles – as surface carriers for
48 potentially toxic species – could significantly affect
49 fetal health and development [20].

50 In this context, the benefit of identifying the ad-
51 sorption mechanism on carbonaceous surfaces and
52 its associated adsorption energy is threefold. It can
53 provide necessary information to better compre-
54 hend, and potentially minimize, the health impact
55 of carbonaceous aerosols. It can help design bet-
56 ter carbon-based materials for industrial use. And
57 finally, it can offer some insights into the complex
58 and still only partially understood soot formation
59 mechanism since adsorption energies define whether
60 the surface species (adsorbates) are chemisorbed or
61 physisorbed, and therefore if the surface molecu-
62 lar compounds result from surface chemistry (rem-
63 nants of the soot formation) or physical condensa-
64 tion [21].

65 Adsorption performances are governed by phys-
66 ical and chemical parameters that greatly vary
67 across adsorbate/adsorbent systems. Thus, a sys-
68 tematic study needs to be undertaken in order to
69 determine i) to what extent the adsorption energy
70 depends on the nature and the size of the adsorbate,
71 and ii) the type of interactions established between
72 adsorbate and adsorbent. Depending upon the na-
73 ture of the adsorbate (gas or liquid) and adsor-
74 bent (polycrystalline film, single-crystal, oxides, or
75 nanoparticle surfaces, powders suspended in a liq-
76 uid or loose powders) [22], various microcalorime-
77 try techniques, such as single-crystal adsorption
78 calorimetry (SCAC), isothermal titration calorime-
79 try (ITC), and differential scanning calorimetry
80 (DSC) [23, 24], or temperature-programmed des-
81 orption (TPD) [25, 26] are commonly used to ei-
82 ther measure directly the heat of adsorption (mi-
83 crocalorimetry) [27–29], or infer the activation en-
84 ergy for desorption (TPD). However, for systems
85 exhibiting meso or macro scale (micrometer- or sub-
86 millimeter sized) inhomogeneities or field-collected
87 samples exhibiting small quantities of matter and
88 complex compositions (*i.e.* with a multitude of
89 co-adsorbed species), the use of these conventional
90 techniques becomes at best arduous and at worst

91 impossible.

92 We propose here an original solution to over-
93 come the restrictions encountered with more con-
94 ventional techniques when determining adsorption
95 energies. Our method relies on laser-induced ther-
96 mal desorption (LITD) coupled with ultra-sensitive
97 mass spectrometry detection. The principle of the
98 method relies on the following stages: the carbona-
99 ceous sample surface is very rapidly heated by a
100 (visible) nanosecond laser pulse. The heating is lo-
101 cal (scale of the laser beam diameter) and transient
102 (initial temperature regained on a microsecond time
103 scale). A fraction of the molecules adsorbed on
104 the sample surface is therefore desorbed and subse-
105 quently ionized by a second (UV) laser pulse before
106 being mass-selectively detected by a time-of-flight
107 mass spectrometer. Low desorption and ionization
108 laser fluences are used to prevent fragmentation of
109 the analytes or alteration of the adsorbent. The
110 fraction of molecules desorbed from an irradiated
111 spot depends on the laser fluence and the number
112 of pulses it is exposed to. These relationships are
113 specific to each adsorbate/adsorbent system and in-
114 dicative of the interaction between the two compo-
115 nents. The resulting experimental data can then be
116 mathematically treated to derive the corresponding
117 adsorption energy.

118 We present in this paper two distinct experimen-
119 tal approaches, derived from the same LITD prin-
120 ciple, along with two mathematical models (and
121 associated statistical procedures) we developed to
122 retrieve the adsorption energy from the recorded
123 experimental data. The method is validated on
124 well-controlled laboratory-synthesized samples, as-
125 sociating several carbonaceous adsorbents and or-
126 ganic/inorganic adsorbates at sub-monolayer con-
127 centration, in a broad range of adsorption energies
128 (0.2 – 1.5 eV).

129 2. Materials and Methods

130 2.1. Experimental approaches

131 Two distinct approaches based on the LITD prin-
132 ciple were followed to collect experimental data for
133 adsorption energy determination: the “signal de-
134 cay” and the “fluence curve”.

135 2.1.1. Signal decay

136 The principle of this first experimental approach
137 is presented in Fig.1a-c: a region of the sample

(delimited by the laser spot on the surface) is irradiated with successive nanosecond laser pulses (10 Hz repetition rate) of constant (low) fluence. For each pulse, a fraction of desorbed molecules is ionized by a second nanosecond laser and further detected by a mass spectrometer. Mass spectra are so recorded for successive laser pulses and the signal corresponding to the adsorbate of interest is plotted as a function of the number of applied laser pulses (Fig. 1c). The pseudo-exponential decay observed simply illustrates a gradual “cleaning” of the irradiated spot by the successive desorption pulses. If this decay is “slow” (*i.e.* a high number of laser pulses is needed to “clean” the surface), then one can infer a strong interaction between the adsorbate and the surface. Conversely, a faster decay (in the same irradiation conditions) will be indicative of looser bonding of the adsorbate to the surface.

2.1.2. Fluence curve

The second approach relies on the variation of the desorption yield with the laser fluence, as illustrated in Fig. 1d-e. In this approach, multiple spots on the sample surface are irradiated with only one pulse each, but the pulses exhibit different fluences. Each measurement is performed on different spots of the sample, *i.e.* on a pristine surface that was not previously irradiated, to ensure that the initial concentration is always the same. The different fluences will lead to different temperature increase for each spot and, consequently to different desorption yields. Fitting the fluence variation of the desorption yield with the adequate equation (see below) allows retrieving the adsorption energy.

2.2. L2MS set-up

The experimental setup used in this work is based on the L2MS technique [11, 30, 31], which combines three key stages: laser desorption (LD), laser ionization (LI), and time-of-flight mass spectrometry (ToF-MS). The sample is mounted onto a copper holder maintained at constant temperature (170 – 190K in this study) by a regulating device consisting of a heating resistor and a liquid nitrogen closed loop. Initially developed for studies on ice samples [32, 33], this system has proved its efficiency in preventing volatile analyte evaporation at the working pressure ($\sim 10^{-8}$ mbar) of the mass spectrometer on many combustion-related [11, 30, 34, 35] or PAH-containing [31, 36] samples.

The sample surface (placed vertically, Fig. 2) is irradiated at normal incidence by the 4 ns pulsed

beam of an Nd:YAG laser (Continuum Minilite, second harmonic, $\lambda = 532$ nm). The desorption laser beam hits the surface with a quasi-top-hat profile of ~ 0.7 mm diameter (measured with a Gentec Beamage-4M beam profiler). The quasi top-hat transverse intensity profile is obtained from the laser output beam by first enlarging it with a beam expander built around a set of convergent and divergent lenses, and then selecting the quasi-flat central region ($\sim 5\%$) of the beam with a diaphragm, which is further image relayed onto the sample surface using a convergent lens.

The desorbed neutral molecules form a forward-peaked plume (*i.e.* narrow angular distribution around the revolution symmetry axis) which propagates at high speed [31, 37] from the sample surface toward the ionization zone. Neutral molecules from the desorbed plume are ionized following a two-photon ionization process [30, 38] using another 4 ns pulsed laser beam (Continuum Powerlite, $\lambda = 266$ nm, 10 Hz repetition rate, ~ 1 mm diameter, top-hat) propagating orthogonally (y direction, Fig. 2) to the desorption plume axis. The ionization laser beam intercepts the desorption plume in between the extraction electrodes of an 1 m long, reflectron time-of-flight mass spectrometer (RM Jordan, mass resolution $m/\Delta m \sim 1000$) at $d \sim 3$ cm from the sample surface. The delay between the desorption and ionization pulses is set to 100 μ s by a digital delay/pulse generator (SRS DG535).

The ions thus generated are extracted and accelerated (x direction) toward the free-field flight tube of the mass spectrometer. Mass spectra are recorded with a digital oscilloscope (LeCroy Waverunner 6200A) at a time resolution of 2 ns/point. Data acquisition is controlled by a dedicated routine developed in LabView (National Instruments). Experimental data points considered in this work and amenable to mathematical treatment represent integrated peak areas corresponding to a given analyte, which includes all the peaks associated with its isotopic distribution.

2.3. Surface evolution upon irradiation

The desorption fluence is carefully adjusted to be in the low, pre-ablation regime [11, 30], which ensures the desorption of neutral species from the surface of the sample without affecting the underlying carbonaceous matrix. Upon irradiation, the sample surface undergoes temperature variations of large magnitude (1500–2000 K) over a

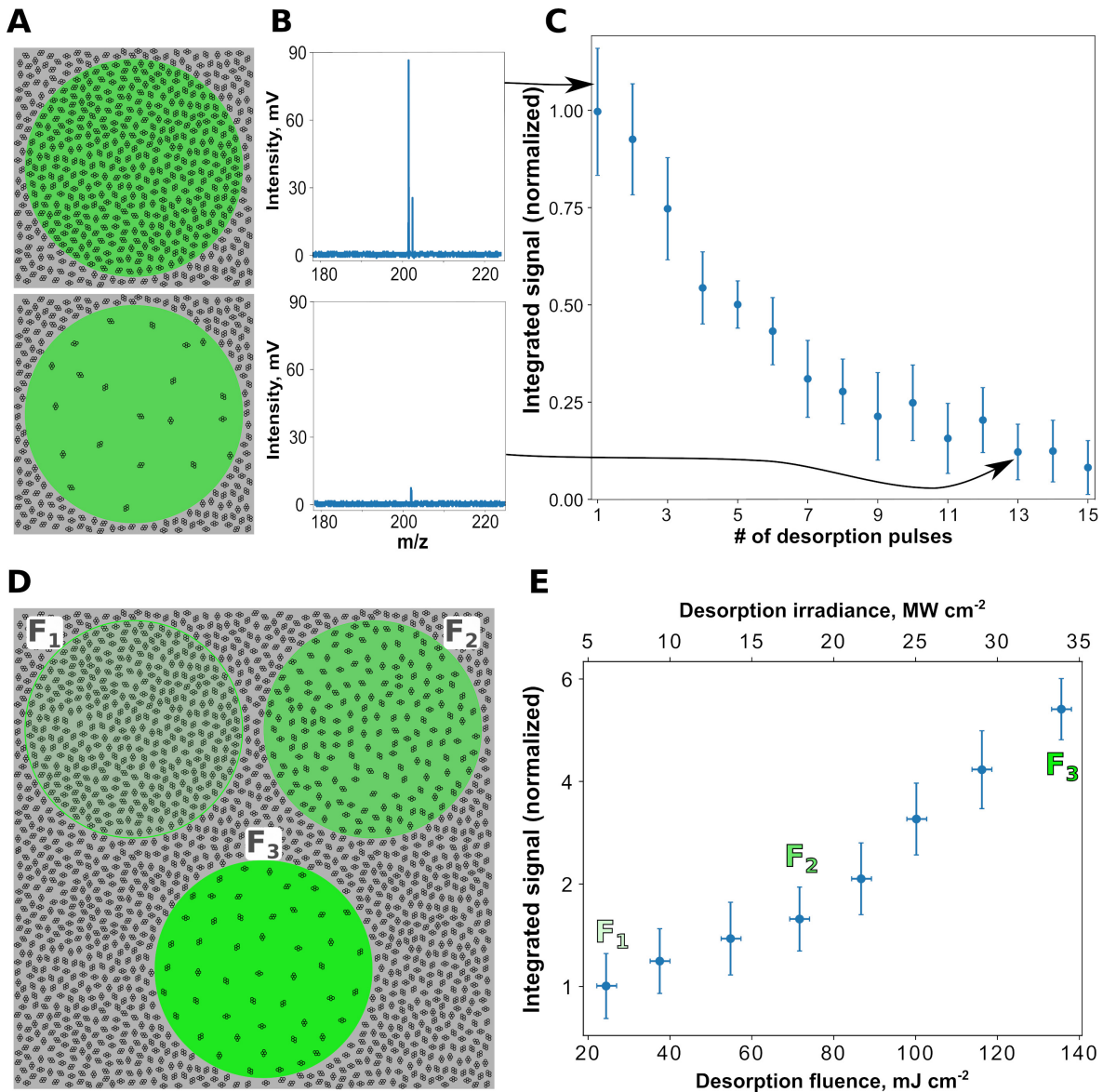


Figure 1: The top and bottom rows describe the “signal decay” and the “fluence curve” experimental approaches, respectively, used to obtain the two distinct datasets from which adsorption energies were subsequently derived. (a) Schematics of the adsorbate coverage evolution upon successive laser pulses of constant fluence applied on the same spot on the sample surface, (b) recorded mass spectra corresponding to two distinct desorption laser pulses (top – 1st pulse, bottom – 13th pulse), and (c) recorded signal decay. (d) Schematics of the “fluence curve” approach – different spots of the sample irradiated with single laser pulses of various fluences, (e) recorded “fluence curve” signal.

238 very short period of time (the surface typically re- 246
 239 gains its initial temperature in about 1 μ s). De- 247
 240 spite the high temperature reached by the surface 248
 241 (for only nanoseconds), it was demonstrated that 249
 242 such a fast-transient process, when generated with 250
 243 low fluence pulses as performed here, does not 251
 244 ablate the adsorbent [11]. Moreover, our fluence op- 252
 245 timization procedure shows that mass spectra are 253

devoid of any fragments originating from the ad-
 sorbate throughout the whole fluence regime used
 in this work. Therefore, our measurements demon-
 strate that such fluence regime prevents the frag-
 mentation of the desorbed molecules and precludes
 ablation of the adsorbent.

In regards to possible adsorbent nanostructure
 rearrangement upon fast-transient heating, previ-

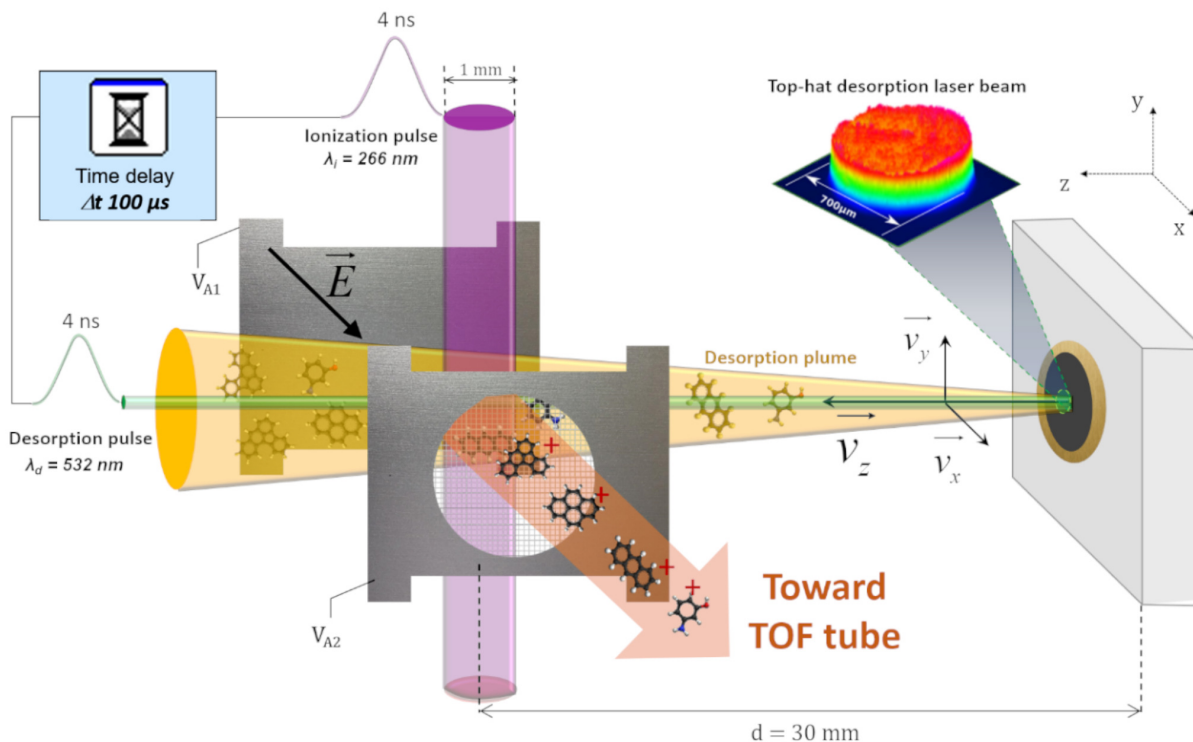


Figure 2: Schematic representation of the laser desorption / laser ionization / ToF-MS experimental arrangement. The desorption laser beam (green) with a top-hat transverse beam profile forms a $700 \mu\text{m}$ spot on the sample surface. The desorbed neutral molecules form a “plume” (dark yellow) which propagates from the sample surface (z axis) toward the ionization region situated in between the extraction electrodes of the ToF-MS. A pulsed UV ionization laser beam (purple, y axis) intersects the desorption plume $100 \mu\text{s}$ after the desorption beam hits the surface. The obtained ions are then extracted and accelerated (x axis) toward the field-free flight tube of the ToF-MS.

ous works on amorphous carbon films [39] or black carbon nanoparticles [40] irradiated by nanosecond Nd:YAG laser pulses showed that no significant change in the sample structure was induced in the low fluence regime (typically $< 50 \text{ mJ cm}^{-2}$). In the work of Abrahamson et al. [40], multi-wavelength pyrometry was used to measure transient surface temperatures of more than 2000°C , while no notable difference in carbon nanostructure was observed by transmission electron microscopy (*i.e.* no rearrangement).

In the first (“signal decay”) experimental approach followed in our work, when a single region of the surface (adsorbent) is irradiated with successive nanosecond laser pulses resulting in the gradual desorption of the adsorbate, it is worth noting that the changing adsorbate surface concentration upon subsequent irradiations does not affect the thermal and optical properties of the system as long as the chemical species are transparent to the desorption

pulse ($\lambda_d = 532 \text{ nm}$) and as the system exhibits a very low surface coverage (both conditions met in this work). As the L2MS technique involves the fast removal of species from the vicinity of the sample [31, 37], re-adsorption of desorbed species is negligible. In addition, any lateral diffusion of molecules across the surface that could potentially replenish the laser spot in between two consecutive desorption laser pulses (100 ms) can be neglected. For instance, it would take minutes for a pyrene molecule to travel a distance of $1 \mu\text{m}$ on a carbon surface [41]. Therefore, the physical characteristics of the sample will not change with the increasing number of desorption pulses and thus not influence the desorption process.

2.4. Sample preparation

The development and validation of a method for adsorption energy determination requires well characterized samples. Moreover, the reproducibility of

the method could be assessed only if the characteristics of the sample are held constant. As this work focuses on desorption from carbonaceous surfaces, combustion-generated particles (soot) would have been an appealing candidate as object of study, however, they usually exhibit a very high variability, as their characteristics (*e.g.* specific surface, porosity) depend highly on the combustion conditions. In this context, laboratory-prepared “synthetic soot” [11] represents an interesting alternative as it exhibits a structure akin to that of real soot but has a known and controllable surface chemical composition.

Synthetic soot is prepared here following the protocol described in our previous work [11]. Briefly, polycyclic aromatic hydrocarbons (pyrene and coronene, Sigma Aldrich, 98% purity) are dissolved into dichloromethane (Sigma Aldrich, 99% purity) to make mother (stock) solutions of known concentrations. To these stock solutions are added activated carbon particles (Pureblack 100 Carbon, average particle diameter 80 nm, specific surface area 80–150 m²g⁻¹) and the resulting mixtures are magnetically stirred for 2 hours. The mixtures are then filtered using a vacuum filtration system employing a quartz fiber filter (Pall Tissuquartz QAT- UP 2500). This filtration step yields, on the one hand, a quartz fiber filter covered by a sub-millimeter thick soot layer infused with the stock solution, and, on the other hand, a filtered solution whose remaining concentration in PAHs can be determined by UV-Vis absorption spectroscopy and subsequent comparison with the stock solution (see Figure S1a). Specifically, as the measured absorbance and the molar concentration are directly proportional in the concentration range studied here, molar concentrations can be estimated knowing the molar extinction coefficient of the solution at a given wavelength and path length. From absorbance measurements of stock solutions of known concentrations can thus be deduced the molar concentrations of the filtered solutions. Therefore, by comparing the absorbance of the stock solution and that of the filtered solution (Figure S1b), it is possible by difference to retrieve the concentration of PAHs remaining on the filter, assuming volatility losses during the preparation steps are negligible [11]. Finally, the surface concentration of PAHs adsorbed on activated carbon particles is calculated knowing the PAH concentration and the specific surface of the particles deposited on the filter.

Three different samples containing either organic

or inorganic species were prepared using the described procedure (Table 1). This included systems containing either a single or two co-adsorbed compounds. Pyrene and coronene were chosen here as adsorbates because of the well-known presence of polycyclic aromatic hydrocarbons (PAH) on the surface of soot particles sampled from real combustors [11, 12]. Additionally, Pb – a heavy metal commonly found in industrial wastewater and usually removed using various carbonaceous materials [9, 10], was used to validate the method for inorganic species. A similar protocol (but a different solvent – ultra-pure deionized water, Purelab Option-Q) was used for the preparation of the lead samples from PbCl₂ salt (Sigma Aldrich, 98%) and Pureblack activated carbon.

Table 1: List of the samples synthesized for adsorption energy measurements. The surface coverage θ (in monolayers, ML) was determined from UV-Vis extinction measurements.

Sample	θ , ML
Pyrene / activated carbon	$2 \cdot 10^{-3}$
(Pyrene + coronene) / activated carbon	$8 \cdot 10^{-3}$ (pyrene) $1.2 \cdot 10^{-2}$ (coronene)
Pyrene / graphite sheet	$\lesssim 10^{-3}$
Pyrene / HOPG	$\lesssim 10^{-3}$
Pb / activated carbon	$\lesssim 10^{-3}$

In order to study the influence of the surface defect density on the retrieved adsorption energy, two more samples based on (mm-thick) graphite sheet and highly oriented pyrolytic graphite (HOPG) adsorbents were prepared in a similar way as the synthetic soot, with the exclusion of the vacuum filtration step. Graphite (Alfa Aesar, graphite sheet) and HOPG (Sigma Aldrich) exhibit significantly lower specific surface areas compared to activated carbon. The resulting adsorbate surface concentration is therefore at the limit of detection of the spectrophotometric method [11]. For this reason, only upper coverage limits ($\sim 10^{-3}$ ML) are provided in Table 1.

Considering the low coverages and the preparation protocol used in this work, we can assume first that no lateral interaction between adsorbate molecules is present, and second that the coverage is homogeneous across the surface. A low coverage also reduces the possibility of adsorbates forming islands of stacked molecules [42] and thus ensures that the only interaction probed is between adsorbates and the adsorbent surface. Moreover, under these experimental conditions any lateral diffusion

385 of molecules across the surface that could poten- 432
386 tially replenish the irradiated spot between desorp- 433
387 tion laser pulses can be neglected [41]. 434

388 2.5. Repeatability 435

389 To account for possible experimental fluctuations 436
390 (mainly due to desorption and ionization lasers), 437
391 several equivalent measurements are performed in 438
392 different zones of the same sample. The ana- 439
393 lyzed regions are chosen not to overlap and there- 440
394 fore all measurements are considered self-contained. 441
395 Specifically, for the first experimental approach 442
396 (signal decay), four signal decays are recorded for 443
397 the same laser set-point, each decay in a pristine 444
398 sample zone. For the second experimental approach 445
399 (*i.e.* fluence curve), four experimental data points 446
400 per desorption fluence value are acquired on four 447
401 distinct (pristine) zones of the sample (*e.g.* for 448
402 pyrene, seven desorption fluence values are utilized 449
403 which results in 28 experimental datapoints in to- 450
404 tal). As all measurements are performed in dif- 451
405 ferent spots on the sample, each datapoint is fully 452
406 independent. Therefore, different combinations of 453
407 these points can be made to build distinct “fluence 454
408 curves”. Among all possible combinations, a to- 455
409 tal of 10 distinct fluence curves are constructed by 456
410 randomly combining experimental datapoints. 457

411 3. Theory 458

412 3.1. Background 459

413 When a pulsed laser beam hits a sample surface, 460
414 a part of its energy (determined by the physical 461
415 properties of the irradiated material) is passed on 462
416 to the sample and induces a temperature jump that 463
417 may i) trigger the desorption of adsorbates possibly 464
418 present on the surface, ii) alter the surface (nanos- 465
419 structure changes), or even iii) ablate micro-volumes 466
420 of sample. This study is performed in the frame- 467
421 work of the first effect, known as laser-induced ther- 468
422 mal desorption (LITD). The pulsed laser-induced 469
423 heating increases the temperature of surfaces at 470
424 high rates (up to $\sim 10^{11}$ K s⁻¹ with a nanosecond 471
425 laser [43]), otherwise unattainable with traditional 472
426 methods (*e.g.* resistive or electron bombardment 473
427 heating), and is therefore appealing for application 474
428 to desorption studies. Early studies showed efficient 475
429 desorption of H, CO, and CO₂ molecules from a 476
430 variety of surfaces irradiated by pulsed laser beams 477
431 [44], phenomenon interpreted as a purely thermal 478
479
480
481
482
483

effect. This effect was later used to study the ad-
sorption and desorption kinetics of these species
by means of relaxation methods [45]. LITD was
also used to examine the desorption of Na and
Cs atoms with a sub-monolayer surface concentra-
tion from Ge (100) substrates [46], of H₂ from Ni
(100), (110) and (111) [45], of CO from Fe [47] and
of benzene from Pt (111) surfaces [48]. However,
none of these studies addressed the determination
of the adsorption energies from LITD data, as they
typically used a single high-fluence laser pulse to
desorb all the adsorbed species from the surface,
thereby completely “cleaning” the irradiated spot
of the sample with only one laser pulse. On the
other hand, when a lower desorption laser fluence
is used, not all the molecules are desorbed by a
single laser pulse and multiple, consecutive pulses
can be applied to the same surface spot [49]. Since
after each desorption pulse the surface concentra-
tion of molecules reduces, the amount of desorbed
compounds decreases after each subsequent laser
pulse, thus resulting in a pseudo-exponential varia-
tion of both surface coverage and desorbed amount.
This variation was first linked to the energetics of
the adsorbate-adsorbent interaction by Specht and
Blades [21], who suggested that the decay obtained
for pyrene desorbing from charcoal corresponds to
molecules that are weakly bound to the surface,
while the relatively constant signal that followed
was associated with molecules having a stronger in-
teraction with the carbonaceous surface. The ob-
served decay, however, was not used by the authors
to derive the strength of the pyrene-surface inter-
action.

A similar decay was reported by our laboratory
in a previous work [11] which focused on the cal-
culation of the detection limit of the two-step laser
mass spectrometry (L2MS) technique. Although
the energetics of the analyte-surface bond was not
studied, we demonstrated at that time that a sin-
gle form of interaction between the analyte and the
carbonaceous surface (in this case physisorption)
can be achieved on surrogate soot samples. A dif-
ferent approach was proposed by Dreisewerd et al.
[50] to derive the activation energy of desorption
from sinapic acid and bovine insulin thick layers
deposited on stainless steel, based on the evolution
of the desorbed amount of molecules with the irra-
diation laser fluence.

The present study builds on this previous works
and proposes for the first time a complete experi-
mental, theoretical, and data treatment methodol-

ogy to derive adsorption energies from LITD/L2MS experiments. Moreover, by developing a theoretical model describing LITD, an extra step was taken toward better understanding fast processes occurring at the sample surface.

3.2. Desorption of physisorbed species

In the kinetic approach, the desorption is described in terms of the desorption rate – the number of molecules that desorb from a unit of surface per unit of time. Assuming that all adsorbed atoms or molecules occupy identical sites, the desorption rate can be expressed by the Polanyi-Wigner equation [51]:

$$-\frac{d\theta}{dt} = \nu\theta^n \exp\left(-\frac{E_{des}}{k_B T}\right) \quad (1)$$

where n is the order of the desorption kinetics (usually $n = 1$ for physisorption), E_{des} is the activation energy for desorption, T is the surface temperature, and k_B the Boltzmann constant. As said above, at the low adsorbate coverages used here (10^{-3} – 10^{-2} monolayers) any interaction between neighbouring adsorbed molecules can be neglected [52], and thus the E_{des} will be characteristic of the adsorbate-adsorbent interaction only. The first-order pre-exponential factor ν (measured in s^{-1}), related with the vibration of the adsorbate-adsorbent bond along the reaction coordinate associated with desorption, is also called attempt frequency and is on the order of the atomic frequency of the crystal lattice ($\sim 10^{13} \text{ s}^{-1}$) [53]. For the atom or molecule to leave the surface it needs to overcome the activation barrier for desorption. Since physisorption is a reversible process, the activation energy of desorption is equal to the adsorption energy: $E_{ads} = E_{des}$, and therefore these two terms will be used interchangeably hereafter.

As seen in Eq. (1), the driving force of desorption is the surface temperature. Therefore, to calculate the rate of desorption and subsequently estimate the adsorption energy, one should first determine the temperature variation. A precise calculation of the temperature temporal and spatial variation involves quite a heavy mathematical apparatus. Therefore, some authors [50, 54, 55] have used a simplified LITD description, a steady-state process involving an “effective” temperature that would be reached upon laser irradiation and at which the desorption occurs.

Although a more elaborated, space- and time-resolved model was developed in this study, we also

present here this simplified approach for the sake of comparison with previous works.

3.3. “Effective temperature” model

The advantage of this simplified, steady-state approach is that all optical and thermal properties of the sample are expressed by a single factor, thus making it easier to retrieve when fitting experimental data. Moreover, the temperature profile of the sample is not required which significantly reduces the computational time needed by the model. Within this approximation, the number of molecules N desorbed after a laser pulse can be expressed as [50, 54, 55]:

$$N \approx A \cdot \exp\left(\frac{-E_{ads}}{k_B (T_0 + BF)}\right) \quad (2)$$

where A is proportional to the surface coverage, B is a factor that describes the conversion of the deposited energy into the surface temperature increase and is associated (for the low coverage used here) solely with the adsorbant properties, T_0 is the initial temperature, F the desorption laser fluence at the surface. In this model, $(T_0 + BF)$ is seen as an “effective” sample temperature which would be reached upon laser irradiation and at which the desorption occurs.

The energy deposited into the sample unit volume is determined by the incident laser fluence, and accounts for the reflectivity R and the optical absorption coefficient $\alpha(\lambda_0)$ of the sample at the desorption laser wavelength λ_0 . This is expressed through the B parameter, as follows [50]:

$$B = (1 - R) \frac{\alpha(\lambda_0)}{\rho c} \quad (3)$$

where c is the specific heat capacity of the sample and ρ is the sample density. The value of the B parameter can considerably change depending on the actual sample characteristics; however, a good initial estimation can be obtained with values reported in the literature. Alternatively, B can be determined by measuring the required physical parameters of the sample prior to the adsorption energy determination. However, this is not always possible in the case of field-collected samples since characterizing micrograms of material can be challenging and adds extra preparation steps that can potentially damage and/or contaminate the sample (often being very expensive to obtain and/or unique). Therefore, the developed model should be

576 able to determine the adsorption energy based on
 577 only an ‘initial guess’ for the B parameter. The B
 578 parameter values calculated for two different adsorbent
 579 materials used in this work (nano-porous soot and graphite),
 580 along with the physical constants used in their calculation,
 581 are presented in Table 2. Note that the B values presented
 582 in this table can be only seen as estimates, sufficiently close
 583 to the real values to be used by the fitting algorithm as
 584 ‘initial guess’.
 585

Table 2: B parameters calculated from Eq. (3) for activated carbon particles and graphite, along with physical parameters sourced from the literature and used in the calculation.

Parameter	Carbonaceous surface	
	Activated carbon particles	Graphite
R	0.2 ^a	0.1 ^b
α , $10^7 m^{-1}$	1.0951 ^{c,d}	3.4385 ^b
ρ , $10^3 kg m^{-3}$	0.4 ^c	1.9 ^d
c , $J K^{-1} kg^{-1}$	840 ^c	970 ^{d,e}
B, $J^{-1} K m^2$	26.0	16.2

^aRef. [56], ^bRef. [57], ^cRef. [11], ^dRef. [58], ^eRef. [59]

586 The surface concentration of adsorbed species decreases
 587 after each desorption pulse, changing the A factor in Eq. (2).
 588 The first laser pulse will give N_1 desorbed molecules:
 589

$$N_1 = p \cdot s \cdot Q_0 \cdot \exp\left(-\frac{E_{ads}}{k_B(T_0 + BF)}\right) \quad (4)$$

590 where Q_0 is the initial adsorbate surface concentration,
 591 s is the surface area of the irradiated spot, and p a
 592 proportionality constant. The number of molecules left on
 593 the irradiated surface spot will progressively decrease after
 594 each subsequent laser pulse.
 595

596 Considering that for the low coverages used here the
 597 adsorption energy does not change with the surface
 598 concentration (see Section 2.4) and the physical properties
 599 of the sample surface do not change upon irradiation with
 600 successive laser pulses (see Section 2.3), N_j molecules will
 601 be desorbed on the j^{th} desorption pulse:
 602

$$N_j = p \cdot s \cdot Q_0 \left(1 - p \cdot \exp\left(-\frac{E_{ads}}{k_B(T_0 + BF)}\right)\right)^{j-1} \cdot \exp\left(-\frac{E_{ads}}{k_B(T_0 + BF)}\right) \quad (5)$$

The S_j signal recorded by the detector will there-

fore be:

$$S_j = m \cdot N_j = m \cdot p \cdot s \cdot Q_0 \left(1 - p \cdot \exp\left(-\frac{E_{ads}}{k_B(T_0 + BF)}\right)\right)^{j-1} \cdot \exp\left(-\frac{E_{ads}}{k_B(T_0 + BF)}\right) \quad (6)$$

603 where m is a proportionality factor accounting for the
 604 ionization efficiency, transfer function of the mass spectrometer,
 605 and detector efficiency.

The variation of the recorded signal can also be expressed
 607 as a function of the desorption fluence – a “fluence curve”
 608 that can be obtained with the second experimental approach
 609 (see Section 2.1.2):

$$S(F) = m \cdot p \cdot s \cdot Q_0 \cdot \exp\left(-\frac{E_{ads}}{k_B(T_0 + BF)}\right) \quad (7)$$

The proposed model can be used to derive the adsorption
 610 energy of a given analyte from experimental data recorded
 611 by the mass spectrometer. The adsorption energy of an
 612 analyte can be retrieved by fitting experimental data either
 613 with Eq. (6) (signal decay induced by successive laser pulses
 614 applied on the same surface spot) or Eq. (7) (signal variation
 615 with fluence). The fitting algorithm requires an “initial
 616 guess” – a starting point relatively close to the actual values.
 617 The initial guess for the B parameter was calculated using
 618 literature data (Table 2). The initial value for the adsorption
 619 energy was also sourced from the literature (*e.g.* 0.98 eV for
 620 pyrene [60, 61]). We note however that fitting the signal
 621 decay and fluence curves with Eq. (6) and (7), respectively,
 622 can be challenging as they contain two highly correlated
 623 parameters. Since the “effective” temperature reached by
 624 the surface upon laser irradiation is significantly higher than
 625 its initial temperature (*i.e.* $BF \gg T_0$), the adsorption
 626 energy E_{ads} and the B parameter are highly correlated.
 627 Therefore, fitting the proposed model to experimental data
 628 requires a specific algorithm which is detailed below in
 629 Section 3.5 and Appendices A and B.
 630
 631
 632
 633
 634

3.4. Transient temperature model

3.4.1. Pulsed laser surface heating

The effective temperature desorption model is only a crude
 635 approximation of the laser-induced thermal desorption and
 636 to fully model this process the fast variation of the sample
 637 temperature

641 should be taken into account. A variety of stud-
642 ies addressed the fast heating of solid samples ex-
643 posed to lasers, describing the processes occurring
644 at different wavelengths, laser irradiances, pulse
645 lengths and on various target materials [11, 49, 62–
646 66]. The approach commonly followed is to de-
647 scribe laser–solid interactions at a macroscopic
648 scale using the heat conduction equation (although
649 some studies treated this phenomenon at an atom-
650 istic/molecular level, but on a limited timescale
651 [54]). For low-fluence nanosecond laser pulses, the
652 energy passed on to the sample does not lead to
653 its melting nor its evaporation, therefore no phase
654 transition terms are needed in the equations [64].
655 Most of the studies focus on the temperature vari-
656 ation in the sample volume (*i.e.* along the z depth
657 axis) and not radially on the surface. Moreover,
658 the laser pulse is often considered as a surface heat
659 source ($z=0$), which does not take into account its
660 propagation into the sample volume as described by
661 the Beer-Lambert law [11].

662 To calculate sample temperature variations upon
663 laser irradiation, the sample was considered as a
664 medium characterized by continuous specific heat
665 capacity c_p , thermal conductivity k and density ρ .
666 Considering a continuum is the approach adopted
667 in all previous studies and is justified by the di-
668 mension of the probed zone (0.7 mm laser diame-
669 ter in our case), which is much larger than possi-
670 ble nanoscale heterogeneities, even for nanoporous
671 media as the synthetic soot samples studied here.
672 Space- and time-resolved temperature profiles were
673 calculated with the 3D heat conduction equation:

$$\rho(T) \cdot c_p(T) \frac{\partial T(x, y, z, t)}{\partial t} = k(T) \left(\frac{\partial^2 T(x, y, z, t)}{\partial x^2} + \frac{\partial^2 T(x, y, z, t)}{\partial y^2} + \frac{\partial^2 T(x, y, z, t)}{\partial z^2} \right) + q_H(x, y, z, t) \quad (8)$$

674 where T is the local sample temperature as a func-
675 tion of the time t and position (x, y, z) . The term
676 $q_H(x, y, z, t)$ describes the heat source which, in this
677 case, is the desorption laser pulse. To match the
678 characteristics of the laser pulse used in the ex-
679 periments, the heat source is represented as a flat
680 space profile (equivalent to a top-hat laser profile)
681 in the calculations. In the temporal domain, the
682 laser beam is represented as a Gaussian pulse. The
683 energy of the laser pulse is absorbed by the sample
684 according to the Beer-Lambert law, therefore:

$$q_H(x, y, z, t) = \alpha I_0 (1 - R) \cdot f(x, y) \cdot g(t) \cdot e^{-\alpha z}$$

$$f(x, y) = \begin{cases} 1, & \sqrt{x^2 + y^2} \leq r_{des} \\ 0, & \text{otherwise} \end{cases} \quad (9)$$

$$g(t) = \frac{1}{\sigma \sqrt{2\pi}} \cdot \exp \left[-\frac{1}{2} \left(\frac{t - t_0}{\sigma} \right)^2 \right], \quad (10)$$

with $\sigma = \frac{\tau_{des}}{2\sqrt{2 \ln 2}}$

685 where R is the sample surface reflectivity, α is the
686 adsorption coefficient at the desorption wavelength
687 (532 nm), I_0 is the pulse peak irradiance. The
688 $f(x, y)$ and $g(t)$ functions define the space and
689 time profiles of the pulsed laser beam of radius r_{des} (top-
690 hat) and duration τ_{des} (full width at half maximum,
691 Gaussian). Previous studies conducted by multi-
692 wavelength pyrometry [40] showed no change in the
693 structural or optical properties of similar carbona-
694 ceous surfaces for a laser-induced transient temper-
695 ature increase of more than 2000°C, which is above
696 the maximum temperatures reached here. Accord-
697 ingly, the R and α parameters were kept constant in
698 the calculations. The same approach is sometimes
699 adopted for simulating the laser-induced incandes-
700 cence (LII) of soot nanoparticles, where even higher
701 temperatures (4000 K) are reached [67]. Moreover,
702 Eqs. (8) and (9) do not include any terms account-
703 ing for phase transitions or surface alteration (*e.g.*
704 photo/thermal-bleaching) [68] as these do not occur
705 at the low desorption fluence values studied here.
706 The boundary conditions required to solve Eq. (8)
707 are:

$$\begin{cases} T(x \rightarrow \infty, y \rightarrow \infty, z \rightarrow \infty, t) = T_i \\ T(x, y, z, t = 0) = T_i \end{cases} \quad (11)$$

708 where T_i is the initial temperature of the sample.

The thermal conductivity of nonporous samples
(*e.g.* graphite) can be found in the literature [58].
For porous materials, such as nano-porous soot
(*nps*), the thermal conductivity k_{nps} strongly de-
pends on the porosity as the efficiency of phonon
propagation is related to the number of contact
points between the nanoparticles forming the sam-
ple. In this case, the thermal conductivity k_{nps} of

the nps layer can be expressed as [69]:

$$k_{nps}(T) = k_{graph}(T) \left[(1 - \xi)^{3/2} + \xi^{1/4} \frac{k_{air}(T)}{k_{graph}(T)} \right] \quad (12)$$

where k_{graph} is the thermal conductivity of bulk graphite [58] and k_{air} is the conductivity of the air filling the pores. The layer porosity ξ is given by:

$$\xi = 1 - \frac{\rho_{nps}}{\rho_{graph}} \quad (13)$$

where ρ_{nps} and ρ_{graph} are the densities of nano-porous soot and graphite, respectively.

The parameters required to calculate the temperature profile of the studied sample were either taken from the literature [11, 26, 58, 63, 69, 70] or calculated from the values for graphite while accounting for the porosity of the sample (Eqs. (12), (13)). The temperature variations of all parameters required for solving Eq. (8) are presented in Fig. S2 of the Supplementary Material. Physical parameters for the graphite sheet and HOPG samples used in this work are nearly identical which allows us to use the same physical characteristics for these two sets of samples.

Eq. (8) was solved with the COMSOL Multiphysics simulation platform using finite element methods. The temporal and spatial temperature evolutions calculated for nano-porous soot and graphite (Fig. 3) show a fast increase with a maximum value reached at $t = 5.5$ ns in the center of the irradiated surface, followed by a slower cooling toward the initial sample temperature (on microsecond timescale). The heat-affected sample depth is in the range of $100 \mu\text{m}$ (Fig. 3b), which is significantly lower than the thickness of the samples used in this study. We note that the obtained depth and temporal profiles follow the same trend as the ones reported by previous similar studies [49, 63, 64], although a direct, quantitative comparison is not possible, as the temperature profiles reported in the literature were computed for different materials and desorption laser characteristics (*e.g.* wavelength, pulse duration, fluence).

3.4.2. Time- and space-resolved desorption

Once the temperature profile $T(x, y, z, t)$ is calculated, a space- and time-resolved desorption mathematical model, including the time-dependence of the desorption rate, the number of molecules desorbed per unit of surface, and the total number of

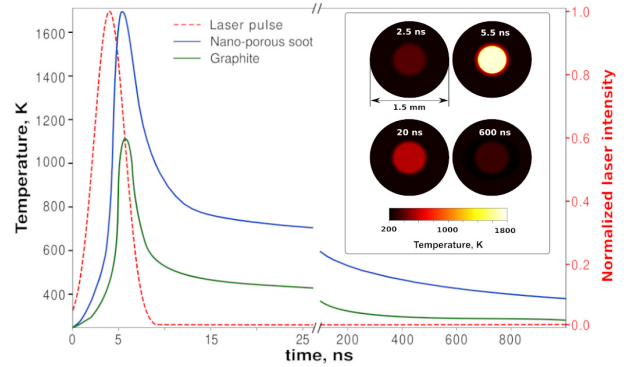


Figure 3: Temporal evolution of the temperature in the center of the irradiated spot ($T(x = 0, y = 0, z = 0, t)$) calculated for nano-porous soot (blue lines) and graphite (green lines) obtained for $F_{des} = 32 \text{ mJ cm}^{-2}$. The temporal profile of the desorption laser is plotted for comparison (red dashed line). Snapshots of the radial distribution of the temperature at various delays after the laser pulse are presented in the inset.

molecules desorbed after each desorption pulse can be formulated.

The number of molecules desorbed from the surface after the first laser pulse can be therefore expressed as follows:

$$N_1 = \iint_{-\infty}^{+\infty} Q_0(x, y) \cdot \left(1 - \exp \left(-\nu \int_0^{\frac{1}{f}} \exp \left(-\frac{E_{ads}}{k_B T(x, y, z = 0, t)} \right) dt \right) \right) dx dy \quad (14)$$

where Q_0 is the initial adsorbate surface concentration and f is the repetition rate of the desorption laser. The number of molecules desorbed on the j^{th} desorption pulse can thus be determined with the following relationship:

$$N_j = \iint_{-\infty}^{+\infty} Q_{j-1}(x, y) \cdot \left(1 - \exp \left(-\nu \int_0^{\frac{1}{f}} \exp \left(-\frac{E_{ads}}{k_B T(x, y, z = 0, t)} \right) dt \right) \right) dx dy \quad (15)$$

$Q_{j-1}(x, y)$ represents the analyte surface concentration after the $(j - 1)^{th}$ desorption pulse (*i.e.* before the j^{th} desorption pulse). Since the surface concentration of the analyte decreases after each desorption pulse, the number of desorbing molecules is progressively reduced.

Once a proportionality factor m is introduced to take into account the overall detection efficiency, the equation can be used for experimental data fitting and adsorption energy retrieval:

$$S_j = m \cdot N_j = m \cdot \iint_{-\infty}^{+\infty} Q_{j-1}(x, y) \cdot \left(1 - \exp \left(-\nu \cdot \int_0^{\frac{1}{f}} \exp \left(-\frac{E_{ads}}{k_B T(x, y, z=0, t)} \right) dt \right) \right) dx dy \quad (16)$$

where S_j is the signal recorded by the detector for the j^{th} desorption pulse. The only unknowns in this equation are the pre-exponential factor ν , the adsorption energy E_{ads} , and the proportionality factor m . Similarly to the “effective temperature” model, the adsorption energy is determined by fitting the experimental data, in this case with Eq. (16). Compared to the “effective temperature” model, the correlation between the unknown parameters in this equation is much lower which facilitates the fitting procedure. Initial adsorption energy values were sourced from the literature and were the same as in the effective temperature model fits (see above). The initial value for the pre-exponential parameter was taken in accordance with literature recommendations [42, 53, 71] as $\nu = 10^{12} \text{ s}^{-1}$.

3.5. Data fitting

Fitting the experimental data can be challenging as some of the unknown parameters (*e.g.* E_{ads} and B in the “effective temperature” model) are highly correlated. Least-square fitting with functions that contain highly correlated parameters and/or multiple exponential functions can be very unstable, as the outcome of the fit is highly dependent on the initial guess. A *search method* [72] could be used in this case – an algorithm relying on multiple least-square fits of the data performed with different initial values (in user-defined ranges) of the unknown parameters. However, this method is characterized by a rather long convergence time and relatively wide posterior distribution of the retrieved values, and thus was not used here. Instead, we adopted a Markov chains Monte Carlo (MCMC) fitting approach (described in Appendix A) in a Bayesian statistics framework. Starting with initial values for fitted parameters sourced from literature (or calculated based on literature data), several hundred thousands fits are generated to match the experimental data using both the steady-state and transient models. This procedure will return posterior distributions for the fitted parameters. The mode

of these distributions will represent the most probable fit for the given dataset and the confidence intervals will reflect the precision of determination of the unknown parameters from the fit. An illustration is given in Fig.4 for the signal decay of pyrene adsorbed on activated carbon nanoparticles (experimental data averaged over four desorption spots on the same sample, 2σ error bars) fitted with the steady-state and the transient temperature models. We notice that both models fit equally well the experimental data, however it is important to emphasize that the red (steady-state model) and green (transient model) dashed lines in Fig. 4a reflect two distinct mathematical concepts. The former results from a severe approximation in that the desorption process occurs at a constant (“effective”) surface temperature, whereas the latter more closely represents the physical reality in that the surface temperature evolves in time and space during the desorption process. The 95% credibility intervals highlighted on the E_{ads} posterior distributions displayed in Fig. 4b clearly reflect the much lower correlation of the fitted parameters in the transient model with respect to the steady-state one. However, these intervals cannot be used directly to derive “physically-significant” error bars for the adsorption energy, as the developed MCMC fitting algorithm could not converge in a reasonable number of steps (500 000) when large error bars are specified for the experimental data. To derive physically-significant error bars of the fitted parameters, we fitted multiple individual datasets generated from the same sample in the same experimental conditions (see Section 2.5) and further applied an “aggregation of estimators” procedure (see Appendix B) to the fitted parameters values and variances.

4. Results

4.1. Polycyclic aromatic hydrocarbons on activated carbon nanoparticles

The experimental approaches and the associated mathematical models are first tested using “synthetic soot” samples synthesized in the laboratory (Section 2.4) by (co)adsorbing polycyclic aromatic hydrocarbons on activated carbon nanoparticles at well-controlled, sub-monolayer surface coverages. Pyrene ($C_{16}H_{10}$) and coronene ($C_{24}H_{12}$) were chosen as representative PAHs as they are both known

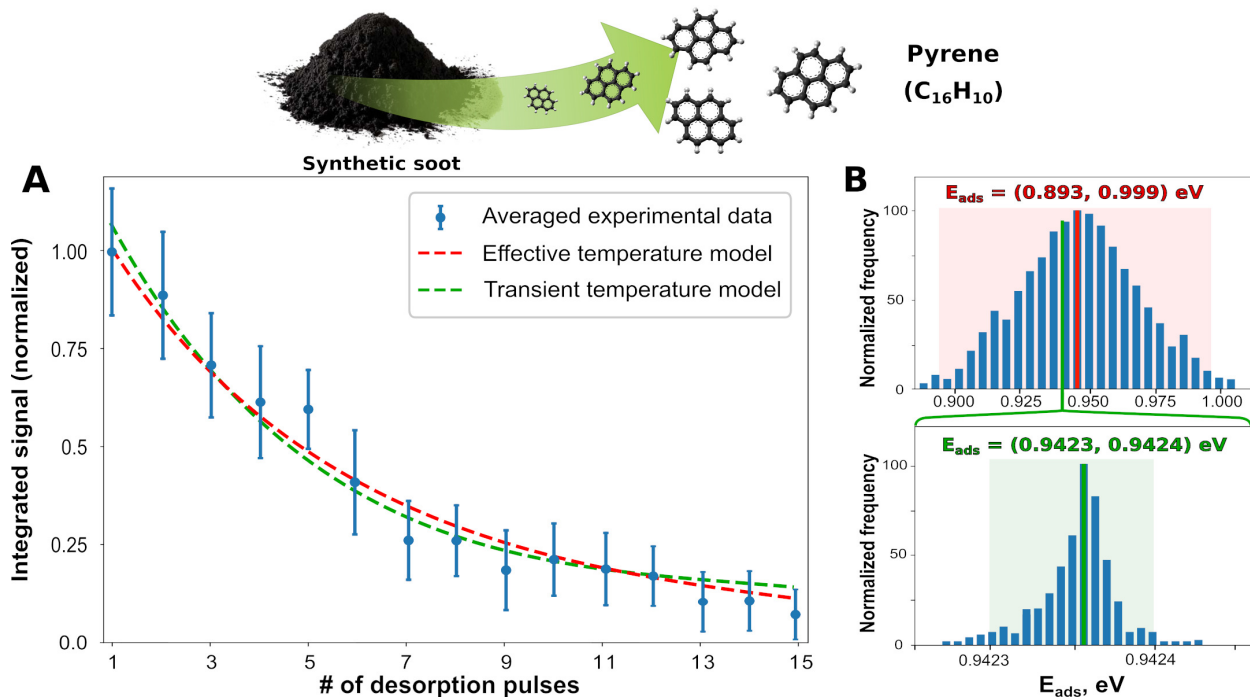


Figure 4: (a) Steady-state (red dashed line) and transient (green dashed line) models fitted to the signal decay curve (four-zone average experimental datapoints) of pyrene desorbing from activated carbon ($F_{des} = 32 \text{ mJ cm}^{-2}$). The plotted fits correspond to the maximum (mode) of the Bayesian posterior distributions shown in (b) – top: steady state, bottom: transient. Shaded areas represent the 95% credibility intervals of E_{ads} .

853 to be present on combustion generated soot parti- 876
 854 cles [11–13, 30] and, at the same time, exhibit signifi- 877
 855 cantly different adsorption energies, which makes 878
 856 them perfect candidates to test the E_{ads} recovery 879
 857 method. Two sets of samples were synthesized, the 880
 858 first one with a single adsorbed PAH (pyrene), the 881
 859 second one with both PAHs co-adsorbed on the 882
 860 same surface. The proposed method allows measur- 883
 861 ing adsorption energies of co-adsorbed species, 884
 862 as the signal of multiple mass peaks can be simulta- 885
 863 neously monitored by time-of-flight mass spectrom- 886
 864 etry.

865 4.1.1. Pyrene

866 Multiple signal decay and fluence curve datasets 890
 867 are recorded from the pyrene / activated carbon 891
 868 surface following the approach described in Sec- 892
 869 tion 2.5 and the MCMC fitting procedure is ap- 893
 870 plied to these individual datasets for both steady- 894
 871 state and transient models. The E_{ads} initial value 895
 872 was taken as 0.98 eV from the literature [60] and 896
 873 this parameter was allowed to vary in the 0.6– 897
 874 1.2 eV interval for both models. For the steady- 898
 875 state model, an initial B value of $26 \text{ J}^{-1} \text{ K m}^2$ (Ta- 899

ble 2) is used, with an allowed variation interval 15–30 $\text{J}^{-1} \text{ K m}^2$. In the transient model, a 10^{12} s^{-1} initial value is considered for the pre-exponential parameter ν in accordance with literature recommendations [53, 71], along with the allowed variation interval 10^{11} – 10^{13} s^{-1} . Starting with these values, a maximum of 100 000 fits are generated to match the individual datasets with the steady-state and transient models. Both models converge before reaching the maximum number of allowed fits, typically in $\sim 50\,000$ steps each. The posterior distributions of the E_{ads} , B , and ν parameters returned by individual fits are aggregated following the procedure described in Appendix B to calculate the average values and associated error bars (1σ) listed in Table 3. The obtained data is then used to reconstruct the signal decay and fluence curves, as illustrated in Fig. S3 of the Supplementary Material.

We notice an excellent agreement between the adsorption energies found in both experimental approaches (both signal decay and fluence curve) and by both models. These results are also well in line with the literature value measured for pyrene ad-

900 sorbed on soot particles using thermal desorption 951
901 kinetics (0.986 eV) [60]. For the “effective temper- 952
902 ature” model the B parameters returned by the 953
903 two approaches ($B_{decay} = 23.9 \pm 3.4 \text{ J}^{-1} \text{ K m}^2$ and 954
904 $B_{fluence} = 21.3 \pm 2.1 \text{ J}^{-1} \text{ K m}^2$) are in good agree- 955
905 ment with each other and slightly smaller than 956
906 the initial estimation ($26 \text{ J}^{-1} \text{ K m}^2$) calculated using 957
907 literature values. For the transient tempera- 958
908 ture model, the retrieved pre-exponential factor ν 959
909 ($1.56 \cdot 10^{12} \text{ s}^{-1}$) is also close to the initial guess.
910 Beside validating the analytical method proposed
911 here, the good agreement with previous works also
912 confirms that the analyzed samples mimic well soot
913 samples described in the literature.

914 4.1.2. Pyrene and coronene co-adsorbed

915 Having demonstrated functionality with a single 965
916 PAH adsorbed onto activated carbon, this adsorp- 966
917 tion energy calculation method is then put to test 967
918 using a system consisting of two different polycyclic 968
919 aromatic compounds co-adsorbed onto the same 969
920 adsorbant but in such low amount ($10^{-3} - 10^{-2}$ 970
921 monolayer) that any lateral interactions between 971
922 them can be neglected. In this configuration, the 972
923 same laser pulse applied to the surface will lead to 973
924 the desorption of both molecules, but each with its 974
925 own kinetics (determined by its adsorption energy 975
926 value). Signals associated with both molecules are 976
927 simultaneously recorded by the mass spectrometer 977
928 to generate individual datasets which are further 978
929 subjected to the fitting procedure described above, 979
930 leading to the results displayed in Table 3. 980

931 For the adsorption energy of pyrene, we observe 981
932 again a very good agreement between the values 982
933 retrieved by the various experimental / theoretical 983
934 approaches and also with the values determined 984
935 above, when pyrene was the sole analyte adsorbed 985
936 onto activated carbon. For coronene, the adsorp- 986
937 tion energy values determined from various ap- 987
938 proaches are in excellent agreement with each other 988
939 and in line with those experimentally determined 989
940 via temperature programmed desorption measure- 990
941 ments for coronene adsorbed on carbon nanofibers 991
942 ($1.31-1.50 \text{ eV}$) [42]. The signal decay and fluence 992
943 curves of both pyrene and coronene reconstructed 993
944 from parameters presented in Table 3 overlaid on 994
945 experimental data are illustrated in Fig. S4 of the 995
946 Supplementary Material. The B parameters (char- 996
947 acteristic of the adsorbent) determined from the 997
948 two fits of the binary adsorbate / activated carbon 998
949 sample are in close agreement with each other and 999
950 also with the ones retrieved for the previous single

adsorbate system (pyrene / activated carbon) shar-
ing the same adsorbent. Similarly, the ν parame-
ter for pyrene agrees well between the two systems.
Coronene shows a higher ν value (with respect to
pyrene), as expected from theoretical calculations
[53, 71]. These results demonstrate the robustness
of the adsorption energy calculation method from
LITD experiments and allow us to conceive its ex-
tension to other adsorbate/adsorbent systems.

960 4.2. Pb on activated carbon nanoparticles

961 Heavy metal ions (*e.g.* Pb^{2+}) are common con- 962
963 taminants of industrial wastewater and are usu- 963
964 ally removed using various carbonaceous materials 964
965 [9, 10]. Thus, the study of the interaction between 965
966 heavy metals, proven to be carcinogenic even at low 966
967 concentration, and materials used for their removal 967
968 from water (*e.g.* activated carbon) is of great im- 968
969 portance. Detection of lead on soot particles (pre- 969
970 sumably coming from combustion of leaded gaso- 970
971 line) was already shown to be possible with laser- 971
972 based mass spectrometry (*e.g.* Particle Analysis 972
973 by Laser Mass Spectrometry, PALMS) employing 973
974 UV ionization of desorbed species [73, 74]. PbCl_2 974
975 salt was dissolved in deionized water and the re- 975
976 sulting solution was used to impregnate the acti- 976
977 vated carbon nanoparticles. Mass spectra recorded 977
978 upon sample irradiation with the 532 nm laser and 978
979 ejecta ionization with the 266 nm laser exhibited 979
980 the characteristic isotopic distribution of Pb^+ in the 980
981 m/z 204–208 range, presented in Fig. S5 of the Sup- 981
982 plementary Material. No Pb^{2+} signal was present 982
983 in the mass spectra. Moreover, experiments per- 983
984 formed with the ionization laser switched off gave 984
985 no signal in the mass spectra, *i.e.* ionized lead is not 985
986 directly sampled from the surface. This may seem 986
987 surprising, as Pb^{2+} ions may be formed in the aque- 987
988 ous solution and be further transferred onto the ad- 988
989 sorbent surface. Our explanation for this is twofold. 989
990 First, the desorption fluence employed (limited by 990
991 the carbonaceous surface ablation threshold) might 991
992 be too low for desorbing these ions from the sur- 992
993 face. Second, the formation of Pb^{2+} in the aqueous 993
994 solution is only one of many other possibilities, as 994
995 Pb-Cl is not a “pure” ionic bond ($\Delta\chi_{\text{Pb-Cl}} < 1.7$). 995
996 Furthermore, in aqueous solution the formation of 996
997 an array of (partially) solvated ions is to be ex- 997
998 pected. All these ions can then adsorb onto acti- 998
999 vated carbon via different mechanisms (adsorption, 999
1000 surface precipitation, ion exchange, sorption, etc.)
[10, 75–79], and participate to further acid/base,

Table 3: Main parameters derived with the “effective” and transient temperature models. Mean values and error bars are computed using the procedure described in Appendix B. The small number of experimental points for the fluence curve of the pyrene/HOPG system prevented a reliable derivation of the adsorption energy from its fluence curve.

Absorbate	Sample	“Effective temp.” model				Transient temp. model	
		Signal decay		Fluence curve		Signal decay	
		E_{ads}, eV	$B, \text{J}^{-1} \text{K m}^2$	E_{ads}, eV	$B, \text{J}^{-1} \text{K m}^2$	E_{ads}, eV	$\nu, 10^{12} \text{s}^{-1}$
Pyrene	Pyrene / activated carbon	0.949 ± 0.049	23.9 ± 3.4	0.968 ± 0.041	21.3 ± 2.1	0.965 ± 0.014	1.56 ± 0.21
	(Pyrene + coronene) / activated carbon	0.961 ± 0.054	20.4 ± 2.8	0.983 ± 0.038	22.4 ± 2.5	0.958 ± 0.018	1.31 ± 0.34
	Pyrene / graphite sheet	0.681 ± 0.019	14.1 ± 1.9	0.662 ± 0.015	15.1 ± 1.4	0.696 ± 0.010	1.24 ± 0.18
	Pyrene / HOPG	0.476 ± 0.021	13.5 ± 1.9	–	–	0.508 ± 0.011	1.38 ± 0.13
Coronene	(Pyrene + coronene) / activated carbon	1.519 ± 0.022	22.8 ± 2.4	1.508 ± 0.024	23.1 ± 1.1	1.513 ± 0.013	2.46 ± 0.15
Pb	Pb / activated carbon	0.226 ± 0.024	20.6 ± 2.3	0.206 ± 0.015	21.1 ± 2.1	0.243 ± 0.011	7.46 ± 0.26

redox or coordination reactions on the particle surface. A thorough investigation of such a complex surface chemistry is well beyond the scope of the present work.

Both experimental approaches (signal decay and fluence curve) were applied to study the desorption of lead from activated carbon particles. For the signal decay approach, the recorded signal vanishes in fewer desorption pulses compared to aromatic species adsorbed on the same adsorbent (Fig. S6, Supplementary Material). Fitting both models to the experimental data resulted in values for the adsorption energy ($E_{ads}^{steady} = 0.226 \text{ eV}$ and $E_{ads}^{transient} = 0.243 \text{ eV}$, Table 3) close to that found in the literature (0.21 eV for Pb(II) adsorbed on carbon particles obtained from bio waste) [10]. A similar value ($E_{ads}^{fluence} = 0.206 \text{ eV}$) was also determined from the fluence curve (Fig. S6, Table 3). The adsorption energy of lead to carbonaceous surfaces is therefore much lower compared to that of aromatic species [10]. The B parameter (which is only related to the adsorbent material) is in good agreement (within the limits of the error bars) with the values returned by the steady-state fits on the other samples involving activated carbon (see Table 3). The pre-exponential factor determined from the transient model fit ($\nu = 7.5 \cdot 10^{12} \text{ s}^{-1}$) is in line with theoretical values calculated for small adsorbates [53]. To the best of our knowledge, no ν experimental value for this system is reported in the literature.

4.3. Toward the systematic exploration of adsorption energies as a function of adsorbent properties

In order to expand the adsorption energy calculation method to systems of much greater chemical or structural complexity, it is first necessary to explore various adsorbate/adsorbent systems ex-

hibiting significantly different adsorption energies. This can be realized by testing either distinct adsorbates on the same adsorbent or, conversely, the same adsorbate on distinct adsorbents, the latter being studied here. The adsorption energy retrieved corresponds to the average energy of all desorbed molecules. If the irradiated surface contains different types of adsorption sites, each one characterized by a different adsorption energy, then the measured E_{ads} can be expressed as a weighted average of all possible energy values (*i.e.* energies that correspond to all existing sites). The change in the proportion of adsorption sites of a given type will modify the average and hence the measured (desorption spot averaged) adsorption energy.

Various surface defects can act as adsorption sites (*e.g.* vacancies, impurities) and most of them are present and abundant on the surface of synthetic (and real) soot particles. The adsorption energy of aromatic compounds on adsorbents exhibiting defect-rich surfaces is higher than that expected when the same compounds are adsorbed on a defect-free carbon lattice [80–83]. Accordingly, as the surfaces of materials such as graphite and HOPG contain a much smaller density of defects compared to activated carbon, the adsorption energy of *e.g.* pyrene, on such adsorbents is expected to be substantially lower.

As predicted, the shape of the signal decay curve and the adsorption energy of pyrene desorbed from a graphite sheet and HOPG are noticeably different (Fig. 5). Since the adsorption energy is lower, a smaller number of laser pulses are required to desorb all molecules present on the irradiated spot, hence a shorter signal decay curve is observed. The adsorption energies obtained from the fits performed with the two models (steady-state and transient) are, once again, very similar. Adsorption en-

ergies obtained for pyrene adsorbed on HOPG (Table 3) are in line with values resulting from ab initio calculations (0.42 – 0.5 eV) [80, 81]. To the best of our knowledge, no experimental measurement for either system (pyrene/HOPG or pyrene/graphite sheet) is reported in the literature. When the adsorbent is graphite sheet, the adsorption energy value obtained for pyrene ranges between the ones retrieved for activated carbon and HOPG, which is expected since the surface contains an intermediate number of defects compared to HOPG (fewer defects) and activated carbon (more defects). It is also possible to obtain “fluence curves” for pyrene desorbing from graphite and retrieve the adsorption energy and B parameter from this approach (Table 3). The values for E_{ads} and B (0.681 eV and $14.1 \text{ J}^{-1} \text{ K m}^2$, respectively) are also in line with the values obtained from the signal decay. Moreover, the obtained B values are close to that calculated with literature parameters ($16.2 \text{ J}^{-1} \text{ K m}^2$, Table 2).

Across the various adsorbate-adsorbent systems investigated here (Table 3), the values obtained and trends followed for B and the pre-exponential ν parameters are in accordance with what should be expected in regards of their relationship with either the adsorbate or the adsorbent. Specifically, as the B parameter is associated with adsorbent properties (for low adsorbate coverages as studied here), its retrieved value should be comparable for all systems featuring the same adsorbent. This is indeed what is observed in Table 3, since a similar B value was obtained with two different experimental approaches for all cases where desorption from the same adsorbent is studied (*e.g.* $20.4 - 23.9 \text{ J}^{-1} \text{ K m}^2$ for activated carbon, Table 3). In contrast, as the pre-exponential factor ν is related to the vibration of the adsorbate-adsorbent bond along the reaction coordinate associated with desorption [53], its value should be largely affected by the adsorbate properties. In accordance, Table 3 shows that the value of this parameter significantly varies for systems based on the same adsorbent but different adsorbates (*e.g.* $1.56 \cdot 10^{12} \text{ s}^{-1}$ for pyrene adsorbed on activated carbon and $7.46 \cdot 10^{12} \text{ s}^{-1}$ for lead adsorbed on activated carbon). Such variation with distinct adsorbates was previously reported [42, 53]. Table 3 also confirms that the pre-exponential factor ν values obtained for desorption events involving the same adsorbate are similar ($1.24 - 1.56 \cdot 10^{12} \text{ s}^{-1}$ for pyrene). Finally, beside the consistent evolution of the retrieved ν values across the systems studied here, they are also in good agreement with

pre-exponential factors previously reported in the literature.

5. Discussion

While it is possible using microcalorimetry to directly appraise the heat of adsorption of a sorbate on various surfaces with a limit of detection (femtomole) akin to ours, performing measurements on such distinct samples (loose powder to highly oriented surfaces) using a single calorimetric technique can be challenging. A direct comparison with microcalorimetry may be impeded by the fact that we do not study adsorption events taking place from a liquid solution nor directly measure the heat of adsorption of a dose of gaseous molecules onto a powder or a surface, but instead monitor the desorption of ‘dry’ adsorbates. Temperature-programmed desorption (TPD) measurements can provide reliable estimates for adsorption energies in experimental conditions close to ours (PAHs already adsorbed on the surface, high vacuum pressure conditions). This technique is thus better suited for comparison purposes. The adsorption energies retrieved using our method are in good agreement with the values reported in the literature from TPD measurements or ab initio calculations. To the best of our knowledge, no adsorption energy values determined via (micro/nano)calorimetry techniques are reported in the literature for the adsorbate/adsorbent systems investigated in this work.

The unique features of the new laser-based method proposed here offer some distinct advantages with respect to the more conventional techniques cited above. First, this method can be applied to systems exhibiting micrometer or sub-millimeter heterogeneities. Specifically, it can be utilized to recover the mean adsorption energy of analytes present in distinct areas of a sample as the lateral resolution is defined by the diameter of the laser spot. The smaller the beam diameter, the better the lateral resolution. Second, our method requires no sample preparation prior to analysis (*e.g.* extraction of material) and necessitates only micrograms of materials to operate. It is hence directly applicable to pristine field-collected and natural samples, for which collecting as much as micrograms of material can be challenging (*e.g.* sampling of aircraft engine [34] or on-road vehicle internal combustion engine emissions [12]). This is particularly important when the focus is on size-selected particles [84, 85] as small as 10 nm, for which the

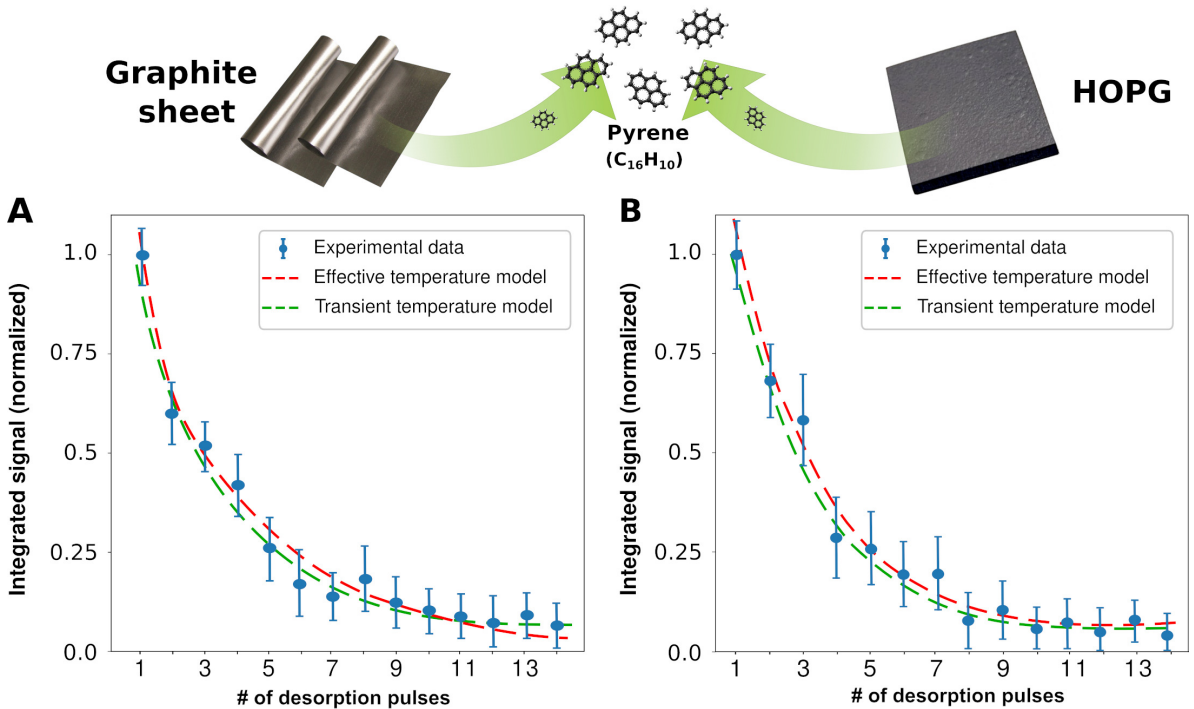


Figure 5: Experimental datapoints (four-zone average) recorded with the “signal decay” approach for pyrene desorbing from (a) graphite sheet ($F_{des} = 50 \text{ mJ cm}^{-2}$) and (b) HOPG ($F_{des} = 61 \text{ mJ cm}^{-2}$). Steady-state (red dashed line) and transient (green dashed line) decay curves calculated with parameters from Table 3.

1178 particle mass lies within the range of attograms. 1202
 1179 Third, it allows the simultaneous study of one or 1203
 1180 several analytes coadsorbed on the same surface, 1204
 1181 which is particularly adapted to real-world complex 1205
 1182 mixtures. Finally, these particular characteristics, 1206
 1183 in conjunction with the very low limit of detection 1207
 1184 (sub-femtomole) that our method provides, consti- 1208
 1185 tute a valuable solution when more conventional 1209
 1186 techniques cannot be utilized. 1210

1187 The method we present is sensitive enough to 1211
 1188 show how the structure of the adsorbent (*e.g.* num- 1212
 1189 ber of defects) can significantly change the mean 1213
 1190 adsorption energy. As expected, the adsorption en- 1214
 1191 ergies derived from our experiments increase with 1215
 1192 the number of surface defects. This method could 1216
 1193 act as a surface defect probe and monitor defect 1217
 1194 densities of various adsorbate/adsorbent systems by 1218
 1195 following a dedicated and systematic experimen- 1219
 1196 tal procedure. Different adsorption energies aver- 1220
 1197 aged over defined zones of a sample surface or 1221
 1198 between distinct samples can further be related to 1222
 1199 the disorder/heterogeneity characteristics using, for in- 1223
 1200 stance, micro-Raman mapping, where deconvoluted 1224
 1201 Raman maps can be superimposed on adsorption 1225

energy maps of the sample surface probed with the 1202
 laser. While currently limited to sub-millimeter 1203
 scale heterogeneities, the lateral resolution could 1204
 be improved by reducing the diameter of the des- 1205
 orption laser spot size. The high sensitivity of the 1206
 technique (ensured by the mass spectrometric de- 1207
 tection) can be used to finely map spatial variations 1208
 of physi/chemisorption interactions across hetero- 1209
 geneous samples, possibly containing small surface 1210
 inclusions (regions with a distinct composition). 1211

The capabilities of the proposed novel method 1212
 open perspectives of application in various fields. 1213
 First, it can serve as a benchmark for adsor- 1214
 bate/adsorbent systems against which other meth- 1215
 ods (*e.g.* ab initio calculations) can be compared. 1216
 On a technological level, it can also encourage the 1217
 development of advanced materials specially de- 1218
 signed to selectively target and capture dangerous 1219
 compounds such as toxins or heavy metal ions [86]. 1220
 Beyond the obvious interest for catalytic or en- 1221
 ergy storage materials [87], this method can also 1222
 be used to characterize thin films grown by phys- 1223
 ical (pulsed laser deposition, magnetron sputter- 1224
 ing) [88] or chemical vapor deposition [89] pro-

cesses, which can (depending on the deposition geometry, substrate etc.) exhibit quite large heterogeneities [90, 91] in their adhesion/adsorption properties. The local character of our technique (defined by the laser beam diameter) in conjunction with a fast mathematical treatment (as the simplified effective temperature model) can help in implementing a real-time, spatially-resolved probe directly in the technological process line. Finally, in the combustion field, our method can help shed light on the formation process of soot particles [92, 93] by identifying the origin of the aromatic species present on the surface (i.e. remnants of the nucleation/growth process or condensation from the gas phase).

6. Conclusions

Employing laser-induced thermal desorption in conjunction with an adequate mathematical framework, we successfully determine the adsorption energy of distinct adsorbates deposited onto various carbonaceous surfaces. We first formulate and then apply two different mathematical equations modeling the desorption phenomena observed experimentally. The first model describes the desorption process as a steady state phenomenon, using an “effective” sample temperature. This model, while greatly simplifying the calculations, also only constitutes a rough approximation of the desorption process. Advantageous when computational speed is required, it can be used in conjunction with real-time chemical mapping to better characterize the zone of interest. The second model accounts for the fast variation of surface temperature triggered by the absorption of the laser pulse energy. This transient temperature model is more complex but mathematically describes a scenario much closer to physical reality, and also benefits from very little correlation between the variables. Both models fit our experimental data well and provide results close to the values reported in the literature. The adsorption energy is determined for two organic molecules (pyrene and coronene) as well as for an inorganic adsorbate (lead). This approach is also able to retrieve the energy of different compounds co-adsorbed on the same sample (from the same measurements). This serves as a good “proof of concept” for the method, demonstrating that laser-induced desorption combined with our mathematical formulations can be used to study adsorption mechanisms. The novelty and the advantages of

the proposed technique over more traditional approaches in some specific cases along with several new perspectives opened by the developed method were discussed.

Supplementary figures Fig. S1 – S6 can be found in the Supplementary Material at [URL will be inserted by publisher].

Acknowledgments

This work was supported by the French National Research Agency (ANR) under contract ANR-18-CE22-0019 (UNREAL) and through the PIA (Programme d’Investissement d’Avenir) under contracts ANR-10-LABX-005 (LABEX CaPPA - Chemical and Physical Properties of the Atmosphere) and ANR-11-LABX-0007-01 (Labex CEMPI - Centre Européen pour les Mathématiques, la Physique et leurs Interactions). The authors acknowledge Prof. B Capoen for providing access to the UV-Vis spectrophotometer at Centre d’Etudes et de Recherches Lasers et Applications (CERLA) platform at the University of Lille.

Author contribution: DD, CF, AF, MZ conceptualized the experimental and theoretical method. DD, MV, YC executed the experiments, DD, CPirim, YC, CF discussed the results, DD, CPirim, CF wrote the initial version of the manuscript, DD, CPirim, CF, CPreda developed and validated the mathematical model and the statistical approach. All authors revised and approved the manuscript.

Appendix A. Markov chains Monte Carlo data fitting

Fitting experimental data with models involving highly correlated parameters requires the use of Bayesian statistics [94–96], which provide powerful tools for estimating complex models where the maximum likelihood-based estimation methods fail. In this framework, several approaches can be followed. Initial tries with the “conventional” *search method* [72] resulted in rather long convergence times and wide posterior distributions of the retrieved parameters (e.g. E_{ads} , B). In this context, we adopted a Markov chains Monte Carlo (MCMC) approach which converges at a much faster pace.

The MCMC method is designed to estimate the joint posterior distribution of a parameter of interest by random sampling in the probability

1321 space. Many problems described by models containing a large number of free parameters, making them expensive to compute with regular methods (e.g. problems in cosmology and astrophysics that deal with low signal-to-noise measurements [94–96]), have benefited from MCMC. One of the most important benefits of Bayesian data analysis is the ability to minimize the impact of nuisance parameters [96] – parameters that are required to model the studied process but otherwise are not the main objective of the fit. Most uses of the MCMC are based on the Metropolis-Hastings (M-H) method [94–96] or its derivatives and consist of three main parts:

- 1335 • Monte Carlo simulations generating random steps to model complex systems.
- 1336
- 1337 • Markov chains - sequences of events that are probabilistically related to one another. Each event originates from a set of outcomes and each outcome determines the next one, in accordance with a fixed set of probabilities.
- 1338
- 1339
- 1340
- 1341
- 1342 • The acceptance-rejection sampling – an iterative algorithm that generates parameter values from their unknown theoretical posterior distribution.
- 1343
- 1344
- 1345

1346 MCMC allows to generate a data subset covering many possible outcomes of a given system in order to obtain an estimate of the theoretical posterior distribution that can be used to extract statistical measures as mean, median or standard deviation. The simulation process is based on a Markov behavior of the iterative algorithm [95, 96]. An example of a model that can benefit from the use of the MCMC algorithm is the laser-induced thermal desorption, e.g. Eq. 6 of the “effective temperature” model that contains a product of two exponential functions and two highly correlated parameters (E_{ads} and B). The performance of the M-H sampler can be very sensitive to the initial choice of parameters. The result of the MCMC fit will be more reliable for longer chains. For this reason, the first values of the Markov chain are usually dropped. Thus, to determine optimal parameters in a data-driven way, a lengthy “burn-in” period must be used. The burn-in allows to start the MCMC procedure with parameters chosen for convenience that might be located in low probability regions, Fig. A.1a. Once the chain has entered the high-probability region, its states become more representative of the correct distribution (the convergence is achieved). All

the values after the convergence are then used to retrieve the distributions and mode values of all parameters, Fig. A.1b.

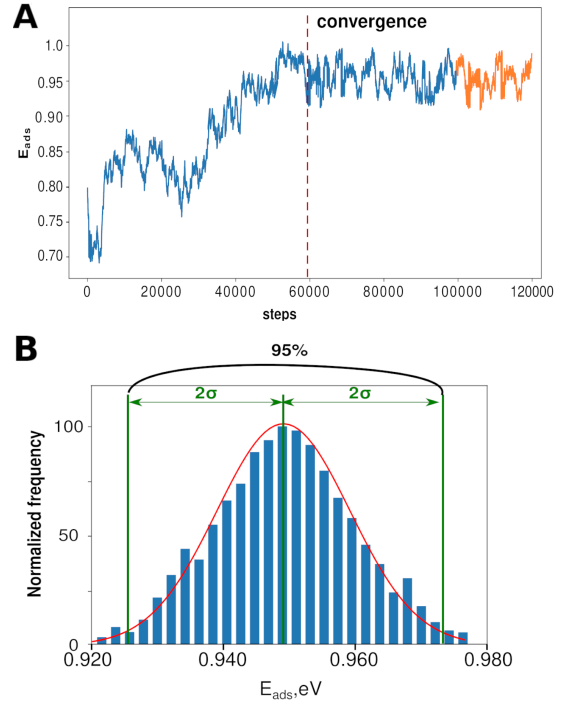


Figure A.1: (a) Example of a Markov chain obtained during fitting of experimental data. The convergence of the fit is depicted with a red dashed line. The last portion of the chain (orange line) is used to determine the posterior distribution of the fitted parameter (b). The distribution is then used to identify the most probable value and the variance of the determined parameter.

Appendix B. Average value and error bar calculation by estimator aggregation

Individual fits performed on multiple independent datasets generated as described in Section 2.5 return estimated values and associated variances for all parameters of interest through the posterior distributions. As an example, Fig. B.1 illustrates the individual fits of four signal decays recorded in the same experimental conditions (the solid lines represent the “most probable fit” (mode) of the Bayesian posterior distribution for each dataset). In order to account for the measurement variability and determine “physically-significant” average values and error bars associated with the fitted parameters (called “estimators” henceforth), the “inter-

1390 nal” (*i.e.* inside one individual dataset) and “exter- 1410
 1391 nal” (*i.e.* between different datasets, such as A, B, 1411
 1392 C, D zones in the signal decay approach, Fig. B.1) 1412
 1393 variances must be combined in an “estimator ag- 1413
 1394 gregation” methodology [97, 98]. 1414

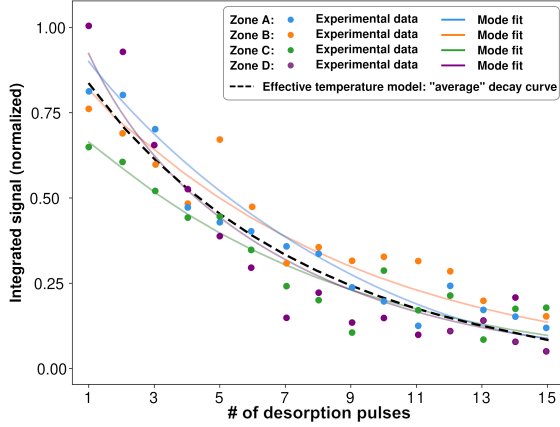


Figure B.1: Symbols: pyrene molecule signal recorded in the same experimental conditions ($F_{des} = 32 \text{ mJ cm}^{-2}$) from four different zones (A, B, C, D) of the same pyrene / activated carbon sample (homogeneous coverage). Solid lines: most probable (mode) fits returned by the Bayesian posterior distribution for each individual dataset. Dashed line: effective temperature model decay curve generated with average parameter values (Table 3).

1395 For a given parameter $\hat{\beta}$, let $\hat{\beta}_i$ be the estima- 1438
 1396 tors obtained from data collected in the zone i , 1439
 1397 $i \in A, B, C, D$. Then, the best linear-combination 1440
 1398 estimator for the $\hat{\beta}$ parameter with respect to the 1441
 1399 mean squared error will be: 1442

$$\hat{\beta} = \sum_{i=1}^n \omega_i \hat{\beta}_i \quad (\text{B.1})$$

1400 where $\omega_i = \frac{\text{Var}^{-1}(\hat{\beta}_i)}{\sum_j \text{Var}^{-1}(\hat{\beta}_j)}$ is the weight associated 1450
 1401 with each estimator, retrieved from fitting individ- 1451
 1402 ual datasets (either signal decays or fluence curves). 1452
 1403 Considering the independence of data recorded in 1453
 1404 different zones of the sample, the standard deviation 1454
 1405 of the $\hat{\beta}$ parameter is given by: 1455

$$\sigma(\hat{\beta}) = \sqrt{\text{Var}(\hat{\beta})} = \sqrt{\sum_i \omega_i^2 (\text{Var}(\hat{\beta}_i) + (\hat{\beta}_i - \hat{\beta})^2)} \quad (\text{B.2})$$

1406 The first term in Eq. (B.2) represents the “inter- 1464
 1407 nal” variance of each dataset, while the second term 1465
 1408 represents the “external” variance (*i.e.* between 1466
 1409 datasets). 1467

The average values and error bars were calculated for the parameters of interest with the described method and reported in Table 3 in the form $\hat{\beta} \pm \sigma(\hat{\beta})$. The validity of the method can be verified with the “average” fitting curve (*i.e.* average for all datasets) calculated with the average values for the required parameters. An example of such a curve obtained with the “effective temperature” model is presented in Fig. B.1 (dashed line).

1419 References

- 1420 [1] T. D. Burchell, Carbon Materials for Advanced Tech- 1421
 1422 nologies, Elsevier Science, Oxford, 1999. doi:10.1016/
 1423 B978-008042683-9/50002-9.
- 1424 [2] A. Jorio, G. Dresselhaus, M. S. Dresselhaus, Car- 1425
 1426 bon Nanotubes. Advanced Topics in the Synthe-
 1427 sis, Structure, Properties and Applications, Springer
 1428 Verlag, Berlin, Heidelberg, 2007. doi:10.1071/
 1429 978-3-540-72865-8.
- 1430 [3] Z. Zhang, S. Yang, H. Li, Y. Zan, X. Li, Y. Zhu,
 1431 M. Dou, F. Wang, Sustainable Carbonaceous Materials
 1432 Derived from Biomass as Metal-Free Electrocatalysts,
 1433 Adv. Mater. 31 (2019) 1805718. doi:10.1002/adma.
 1434 201805718.
- 1435 [4] M. Inagaki, F. Kang, M. Toyoda, H. Konno, Car-
 1436 bon Materials for Adsorption of Molecules and
 1437 Ions, Adv. Mate. 5 (2014) 335–361. doi:10.1016/
 1438 b978-0-12-407789-8.00015-6.
- 1439 [5] M. R. Elamin, B. Y. Abdulkhair, A. O. Elzupir, Insight
 1440 to aspirin sorption behavior on carbon nanotubes from
 1441 aqueous solution: Thermodynamics, kinetics, influence
 1442 of functionalization and solution parameters, Sci. Rep.
 1443 9 (2019) 12795. doi:10.1038/s41598-019-49331-6.
- 1444 [6] M. Ahmaruzzaman, D. Mohanta, A. Nath, Environ-
 1445 mentally benign fabrication of SnO₂-CNT nanohy-
 1446brids and their multifunctional efficiency as an adsor-
 1447 bent, catalyst and antimicrobial agent for water decon-
 1448 tamination, Sci. Rep. 9 (2019) 12795. doi:10.1038/
 1449 s41598-019-49181-2.
- 1450 [7] S. T. Lim, J. H. Kim, C. Y. Lee, S. Koo, D. Jerng,
 1451 S. Wongwises, H. S. Ahn, Mesoporous graphene adsor-
 1452 bents for the removal of toluene and xylene at various
 1453 concentrations and its reusability, Sci. Rep. 9 (2019)
 1454 10922. doi:10.1038/s41598-019-47100-z.
- 1455 [8] M. Darvish Ganji, H. Kiyani, Molecular simulation
 1456 of efficient removal of H₂S pollutant by cyclodextrine
 1457 functionalized CNTs, Sci. Rep. 9 (2019) 10605. doi:
 1458 10.1038/s41598-019-46816-2.
- 1459 [9] A. A. Abia, E. D. Asuquo, Lead (II) and nickel (II)
 1460 adsorption kinetics from aqueous metal solutions using
 1461 chemically modified and unmodified agricultural adsor-
 1462 bents, Afr. J. Biotechnol. 5 (2006) 1475–1482.
- 1463 [10] R. Ahmad, S. Haseeb, Adsorption of Pb(II) on Men-
 1464 tha piperita carbon (MTC) in single and quaternary
 1465 systems, Arab. J. Chem. 10 (2017) S412–S421. doi:
 1466 10.1016/j.arabjc.2012.09.013.
- 1467 [11] A. Faccinetto, C. Focsa, P. Desgroux, M. Ziskind,
 1468 Progress toward the Quantitative Analysis of PAHs
 Adsorbed on Soot by Laser Desorption/Laser
 Ionization/Time-of-Flight Mass Spectrometry,

- Environ. Sci. Technol. 49 (2015) 10510–10520. doi:10.1021/acs.est.5b02703.
- [12] O. B. Popovicheva, C. Irimiea, Y. Carpentier, I. K. Ortega, E. D. Kireeva, N. K. Shonija, J. Schwarz, M. Vojtíšek-Lom, C. Focsa, Chemical composition of diesel/biodiesel particulate exhaust by FTIR spectroscopy and mass spectrometry: Impact of fuel and driving cycle, *Aerosol Air Qual. Res.* 17 (2017) 1717–1734. doi:10.4209/aaqr.2017.04.0127.
- [13] P. Parent, C. Laffon, I. Marhaba, D. Ferry, T. Z. Regier, I. K. Ortega, B. Chazallon, Y. Carpentier, C. Focsa, Nanoscale characterization of aircraft soot: A high-resolution transmission electron microscopy, Raman spectroscopy, X-ray photoelectron and near-edge X-ray absorption spectroscopy study, *Carbon* 101 (2016) 86–100. doi:10.1016/j.carbon.2016.01.040.
- [14] D. L. Diggs, K. L. Harris, P. V. Rekhadevi, A. Ramesh, Tumor microsomal metabolism of the food toxicant, benzo(a)pyrene, in *Apc^{Min}* mouse model of colon cancer, *Tumor. Biol.* 33 (2012) 1255–1260. doi:10.1007/s13277-012-0375-6.
- [15] K. H. Kim, S. A. Jahan, E. Kabir, R. J. C. Brown, A review of airborne polycyclic aromatic hydrocarbons (PAHs) and their human health effects, *Environ. Int.* 60 (2013) 71–80. doi:10.1016/j.envint.2013.07.019.
- [16] G. Grimmer, *Environmental carcinogens: Polycyclic aromatic hydrocarbons: Chemistry, occurrence, biochemistry, carcinogenicity*, CRC Press, New York, 2018. doi:10.1201/9781351071758.
- [17] C. A. Pope, D. W. Dockery, Health effects of fine particulate air pollution: Lines that connect, *J. Air Waste Manage. Assoc.* 56 (2006) 709–742. doi:10.1080/10473289.2006.10464485.
- [18] B. A. Maher, I. A. Ahmed, V. Karloukovski, D. A. MacLaren, P. G. Foulds, D. Allsop, D. M. Mann, R. Torres-Jardón, L. Calderon-Garciduenas, Magnetite pollution nanoparticles in the human brain, *Proc. Natl. Acad. Sci. U.S.A.* 113 (2016) 10797–10801. doi:10.1073/pnas.1605941113.
- [19] N. D. Saenen, H. Bové, C. Steuwe, M. B. Roeffaers, E. B. Provost, W. Lefebvre, C. Vanpoucke, M. Ameloot, T. S. Nawrot, Children’s urinary environmental carbon load: A novel marker reflecting residential ambient air pollution exposure?, *Am. J. Respir. Crit. Care Med.* 196 (2017) 873–881. doi:10.1164/rccm.201704-0797OC.
- [20] H. Bové, E. Bongaerts, E. Slenders, E. M. Bijmens, N. D. Saenen, W. Gyselaers, P. V. Eyken, M. Plusquin, M. B. J. Roeffaers, M. Ameloot, T. S. Nawrot, Ambient black carbon particles reach the fetal side of human placenta, *Nat. Commun.* 10 (2019) 3866. doi:10.1038/s41467-019-11654-3.
- [21] A. A. Specht, M. W. Blades, Direct determination of polycyclic aromatic hydrocarbons in solid matrices using laser desorption/laser photoionization ion trap mass spectrometry, *J. Am. Soc. Mass Spectrom.* 14 (2003) 562–570. doi:10.1016/S1044-0305(03)00143-0.
- [22] L. Basta, S. Veronesi, Y. Murata, Z. Dubois, N. Mishra, F. Fabbri, C. Coletti, S. Heun, A sensitive calorimetric technique to study energy (heat) exchange at the nanoscale, *Nanoscale* 10 (2018) 10079–10086. doi:10.1039/C8NR00747K.
- [23] C. T. Campbell, J. R. Sellers, Enthalpies and entropies of adsorption on well-defined oxide surfaces: Experimental measurements, *Chem. Rev.* 113 (2013) 4106–4135. doi:10.1021/cr300329s.
- [24] A. Saha, A simultaneous volumetric adsorption–isothermal titration calorimetry study of small molecules on supported metallic nanoparticles, *J. Therm. Anal. Calorim.* 124 (2016) 1623–1634. doi:10.1007/s10973-016-5262-8.
- [25] J. L. Falconer, J. A. Schwarz, Temperature-programmed desorption and reaction: applications to supported catalysts, *Cat. Rev.* 25 (1983) 141–227. doi:10.1080/01614948308079666.
- [26] R. A. Ketola, J. T. Kiuru, V. Tarkiainen, J. T. Kokkonen, J. Räsänen, T. Kotiaho, Detection of volatile organic compounds by temperature-programmed desorption combined with mass spectrometry and fourier transform infrared spectroscopy, *Anal. Chim. Acta.* 562 (2006) 245–251. doi:10.1016/j.aca.2006.01.069.
- [27] J. T. Stuckless, D. E. Starr, D. J. Bald, C. T. Campbell, J. T. Stuckless, D. E. Starr, D. J. Bald, C. T. Campbell, Metal adsorption calorimetry and adhesion energies on clean single-crystal surfaces Metal adsorption calorimetry and adhesion energies on clean single-crystal surfaces, *J. Chem. Phys.* 107 (1997) 5547–5553. doi:10.1063/1.474230.
- [28] W. A. Brown, R. Kose, D. A. King, Femtomole Adsorption Calorimetry on Single-Crystal Surfaces, *Chem. Rev.* 98 (1998) 797–831. doi:10.1021/cr9700890.
- [29] J. H. Fischer-Wolfarth, J. A. Farmer, J. M. Flores-Camacho, A. Genest, I. V. Yudanov, N. Rösch, C. T. Campbell, S. Schauermann, H.-J. Freund, Particle-size dependent heats of adsorption of CO on supported Pd nanoparticles as measured with a single-crystal microcalorimeter, *Phys. Rev. B* 81 (2010) 241416. doi:10.1103/PhysRevB.81.241416.
- [30] A. Faccinetto, P. Desgroux, M. Ziskind, E. Therssen, C. Focsa, High-sensitivity detection of polycyclic aromatic hydrocarbons adsorbed onto soot particles using laser desorption/laser ionization/time-of-flight mass spectrometry: An approach to studying the soot inception process in low-pressure flames, *Combust. Flame* 158 (2011) 227–239. doi:10.1016/j.combustflame.2010.08.012.
- [31] C. Miheșan, M. Ziskind, E. Therssen, P. Desgroux, C. Focsa, IR laser resonant desorption of polycyclic aromatic hydrocarbons, *Chem. Phys. Lett.* 423 (2006) 407–412. doi:10.1016/j.cplett.2006.04.032.
- [32] C. Focsa, J. Destombes, Na/K (H₂O) n clusters produced by laser desorption of Na/K salt doped ice, *Chemical Physics Letters* 347 (2001) 390–396. doi:10.1016/S0009-2614(01)01068-5.
- [33] C. Miheșan, N. Lebrun, M. Ziskind, B. Chazallon, C. Focsa, J. Destombes, Ir laser resonant desorption of formaldehyde–H₂O ices: hydrated cluster formation and velocity distribution, *Surf. Sci.* 566 (2004) 650–658. doi:10.1016/j.susc.2004.06.128.
- [34] D. Delhayé, F. X. Ouf, D. Ferry, I. K. Ortega, O. Penanhoat, S. Peillon, F. Salm, X. Vancassel, C. Focsa, C. Irimiea, N. Harivel, B. Perez, E. Quinton, J. Yon, D. Gaffie, The MERMOSE project: Characterization of particulate matter emissions of a commercial aircraft engine, *J. Aerosol Sci.* 105 (2017) 48–63. doi:10.1016/j.jaerosci.2016.11.018.
- [35] L. D. Ngo, D. Duca, J. A. Noble, A. R. Ikhenazene, M. Vojkovic, Y. Carpentier, C. Irimiea, Chemical discrimination of the particulate and gas phases of mini-CAST exhausts using a two-filter collection method, *Atmospheric Measurement Techniques* 13 (2020) 951–967.

- doi:10.5194/amt-13-951-2020. 1664
- [36] C. Mihean, M. Ziskind, E. Therssen, P. Desgroux, 1665
C. Focsa, Parametric study of polycyclic aromatic hydrocarbon laser desorption, *Journal of Physics: Condensed Matter* 20 (2007) 025221. doi:10.1088/0953-8984/20/02/025221. 1666
- [37] A. Poretzky, D. Geohegan, G. Hurst, M. Buchanan, 1667
B. Luk'yanchuk, Imaging of vapor plumes produced by matrix assisted laser desorption: a plume sharpening effect, *Phys. Rev. Lett.* 83 (1999) 444. doi:10.1103/PhysRevLett.83.444. 1668
- [38] R. Zimmermann, M. Blumenstock, H. J. Heger, K. W. 1669
Schramm, A. Kettrup, Emission of nonchlorinated and chlorinated aromatics in the flue gas of incineration plants during and after transient disturbances of combustion conditions: Delayed emission effects, *Environ. Sci. Technol.* 35 (2001) 1019–1030. doi:10.1021/es0001431. 1670
- [39] E. Cappelli, C. Scilletta, S. Orlando, V. Valentini, 1671
M. Servidori, Laser annealing of amorphous carbon films, *Appl. Surf. Sci.* 255 (2009) 5620–5625. doi:10.1016/j.apsusc.2008.10.062. 1672
- [40] J. P. Abrahamson, M. Singh, J. P. Mathews, R. L. Vander Wal, Pulsed laser annealing of carbon black, *Carbon* 124 (2017) 380–390. doi:10.1016/j.carbon.2017.08.080. 1673
- [41] S. Ahn, D. Werner, H. K. Karapanagioti, D. R. McGlothlin, R. N. Zare, R. G. Luthy, Phenanthrene and pyrene sorption and intraparticle diffusion in polyoxymethylene, coke, and activated carbon, *Environ. Sci. Technol.* 39 (2005) 6516–6526. doi:10.1021/es050113o. 1674
- [42] R. Zacharia, H. Ulbricht, T. Hertel, Interlayer cohesive energy of graphite from thermal desorption of polycyclic aromatic hydrocarbons, *Phys. Rev. B* 69 (2004) 155406. doi:10.1103/PhysRevB.69.155406. 1675
- [43] R. J. Beuhler, E. Flanigan, L. J. Greene, L. Friedman, 1676
Proton transfer mass spectrometry of peptides: rapid heating technique for underivatized peptides containing arginine, *J. Am. Chem. Soc.* 96 (1974) 3990–3999. doi:10.1021/ja00819a043. 1677
- [44] L. P. Levine, J. F. Ready, E. Bernal, Gas desorption produced by a giant pulse laser, *J. Appl. Phys.* 38 (1967) 331–336. doi:10.1063/1.1708977. 1678
- [45] K. Christmann, O. Schober, G. Ertl, M. Neumann, Adsorption of hydrogen on nickel single crystal surfaces, *The Journal of Chemical Physics* 4528 (1974) 4528–4540. doi:10.1063/1.1680935. 1679
- [46] J. M. Chen, C. C. Chang, Laser desorption of submonolayers of Na and Cs from Ge substrates, *J. Appl. Phys.* 43 (1972) 3884–3886. doi:10.1063/1.1661832. 1680
- [47] G. Wedler, H. Ruhmann, Laser induced thermal desorption of carbon monoxide from Fe(110) surfaces, *Surf. Sci.* 121 (1982) 464–486. doi:10.1016/0039-6028(82)90255-2. 1681
- [48] H. Arnolds, C. Rehbein, G. Roberts, R. J. Levis, D. A. King, Femtosecond Near-Infrared Laser Desorption of Multilayer Benzene on Pt(111): A Molecular Newton's Cradle?, *J. Phys. Chem. B* 104 (2002) 3375–3382. doi:10.1021/jp993688e. 1682
- [49] J. L. Brand, S. M. George, Effects of laser pulse characteristics and thermal desorption parameters on laser induced thermal desorption, *Surf. Sci.* 167 (1986) 341–362. doi:10.1016/0039-6028(86)90709-0. 1683
- [50] K. Dreisewerd, M. Schürenberg, M. Karas, F. Hillenkamp, Influence of the laser intensity and spot size on the desorption of molecules and ions in matrix-assisted laser desorption/ionization with a uniform beam profile, *Int. J. Mass Spectrom. Ion Process.* 141 (1995) 127–148. doi:10.1016/0168-1176(94)04108-J. 1684
- [51] K. Oure, V. G. Lifshits, A. A. Saranin, A. V. Zotov, M. Katayama, *Surface Science: An Introduction*, Springer, Berlin, 2003. 1685
- [52] R. M. Bouglas, *Principles of adsorption and adsorption processes*, Wiley-Interscience publication, New York, 1984. 1686
- [53] K. Christmann, *Introduction to Surface Physical Chemistry*, Springer, Heidelberg, 1991. 1687
- [54] L. V. Zhigilei, B. J. Garrison, Molecular dynamics simulation study of the fluence dependence of particle yield and plume composition in laser desorption and ablation of organic solids, *Appl. Phys. Lett.* 74 (1999) 1341–1343. doi:10.1063/1.123544. 1688
- [55] S. Kuper, J. Brannon, K. Brannon, Threshold behavior in polyimide photoablation: Single-shot rate measurements and surface-temperature modeling, *Appl. Phys. A* 56 (1993) 43–50. doi:10.1007/BF00351902. 1689
- [56] W. H. Dalzell, a. F. Sarofim, Optical Constants of Soot and Their Application to Heat-Flux Calculations, *J. Heat Transfer* 91 (1969) 100. doi:10.1115/1.3580063. 1690
- [57] A. B. Djurišić, E. H. Li, Optical properties of graphite, *J. Appl. Phys.* 85 (1999) 7404–7410. doi:10.1063/1.369370. 1691
- [58] R. J. M. Konings, *Comprehensive Nuclear Materials, Material Properties - Oxide Fuels for Light Water Reactors and Fast Neutron Reactors*, Elsevier, Amsterdam, 2012. doi:10.1016/B978-0-08-056033-5.90001-6. 1692
- [59] A. Butland, R. Maddison, The specific heat of graphite: an evaluation of measurements, *J. Nucl. Mater.* 49 (1973) 45–56. doi:10.1016/0022-3115(73)90060-3. 1693
- [60] A. Guilloateau, M. L. Nguyen, Y. Bedjanian, G. Le Bras, Desorption of polycyclic aromatic hydrocarbons from soot surface: Pyrene and fluoranthene, *J. Phys. Chem. A* 112 (2008) 10552–10559. doi:10.1021/jp803043s. 1694
- [61] Y. Bedjanian, M. L. Nguyen, A. Guilloateau, Desorption of polycyclic aromatic hydrocarbons from soot surface: Five- and six-ring (C₂₂, C₂₄) PAHS, *J. Phys. Chem. A* 114 (2010) 3533–3539. doi:10.1021/jp912110b. 1695
- [62] A. Bogaerts, Z. Chen, R. Gijbels, A. Vertes, Laser ablation for analytical sampling: what can we learn from modeling?, *Spectrochim. Acta B* 58 (2003) 1867–1893. doi:10.1016/j.sab.2003.08.004. 1696
- [63] D. Burgess Jr., P. C. Stair, E. Weitz, Calculations of the surface temperature rise and desorption temperature in laser-induced thermal desorption, *J. Vac. Sci. Technol. A* 4 (1986) 1362–1366. doi:10.1116/1.573571. 1697
- [64] P. C. Stair, E. Weitz, Pulsed-laser-induced desorption from metal surfaces, *J. Opt. Soc. Am. B* 4 (1987) 255–260. doi:10.1364/JOSAB.4.000255. 1698
- [65] J. Ho, C. Grigoropoulos, J. Humphrey, Computational study of heat transfer and gas dynamics in the pulsed laser evaporation of metals, *J. Appl. Phys.* 78 (1995) 4696–4709. doi:10.1063/1.359817. 1699
- [66] J. Bechtel, Heating of solid targets with laser pulses, *J. Appl. Phys.* 46 (1975) 1585–1593. doi:10.1063/1.321760. 1700
- [67] E. V. Gurentsov, A review on determining the refractive index function, thermal accommodation coefficient and evaporation temperature of light-absorbing nanoparticles suspended in the gas phase using the laser-induced incandescence, *Nanotechnol. Rev.* 7 (2018) 583–604. 1701

- doi:10.1515/ntrev-2018-0080. 1794
- [68] J. P. Cummings, J. T. Walsh Jr, Erbium laser ablation: 1795
the effect of dynamic optical properties, *Appl. Phys. Lett.* 62 (1993) 1988–1990. doi:10.1063/1.109512. 1796
- [69] W. D. Ciro, E. G. Eddings, A. F. Sarofim, Experimental 1798
and numerical investigation of transient soot buildup 1799
on a cylindrical container immersed in a jet fuel pool 1800
fire, *Combust. Sci. Technol.* 178 (2006) 2199–2218. doi: 1801
10.1080/00102200600626108. 1802
- [70] C. Pradère, J.-C. Batsale, J.-M. Goyhénèche, R. Pailler, 1803
S. Dilhaire, Thermal properties of carbon fibers at very 1804
high temperature, *Carbon* 47 (2009) 737–743. doi:10. 1805
1016/j.carbon.2008.11.015. 1806
- [71] K. A. Fichthorn, R. A. Miron, Thermal desorption of 1807
large molecules from solid surfaces, *Phys. Rev. Lett.* 89 1808
(2002) 196103. doi:10.1103/PhysRevLett.89.196103. 1809
- [72] X. L. Han, Monte Carlo Least-Squares Fitting of Ex- 1810
perimental Signal Waveforms Random Walk Method 1811
Testing the Fitting Algorithm, *J. Comput. Sci.* 4 1812
(2006) 1548–1555, URL: [https://digitalcommons. 1813](https://digitalcommons.butler.edu/facsch_papers/750)
[butler.edu/facsch_papers/750](https://digitalcommons.butler.edu/facsch_papers/750). 1814
- [73] S. H. Lee, D. M. Murphy, D. S. Thomson, A. M. Mid- 1815
dlebrook, Chemical components of single particles mea- 1816
sured with particle analysis by laser mass spectrome- 1817
try (PALMS) during the Atlanta supersite project: Fo- 1818
cus on organic/sulfate, lead, soot, and mineral par- 1819
ticles, *J. Geophys. Res.* 107 (2002) AAC1–13. doi: 1820
10.1029/2000JD000011. 1821
- [74] Y. Zhang, X. Wang, H. Chen, X. Yang, J. Chen, 1822
J. O. Allen, Source apportionment of lead-containing 1823
aerosol particles in shanghai using single particle mass 1824
spectrometry, *Chemosphere* 74 (2009) 501–507. doi: 1825
10.1016/j.chemosphere.2008.10.004. 1826
- [75] M. Sekar, V. Sakthi, S. Rengaraj, Kinetics and equilib- 1827
rium adsorption study of lead (II) onto activated car- 1828
bon prepared from coconut shell, *J. Colloid Interface 1829*
Sci. 279 (2004) 307–313. doi:10.1016/j.jcis.2004. 1830
06.042. 1831
- [76] T. A. Saleh, Nanocomposite of carbon nanotubes/silica 1832
nanoparticles and their use for adsorption of Pb(II): 1833
from surface properties to sorption mechanism, *Des- 1834*
alination Water Treat. 57 (2016) 10730–10744. doi: 1835
10.1080/19443994.2015.1036784. 1836
- [77] E. Bottani, J. M. Tascon, Adsorption of Inorganic 1837
Species from Aqueous Solutions. Adsorption by Car- 1838
bon, Elsevier, Amsterdam, 2008. doi:10.1016/ 1839
B978-0-08-056033-5.90001-6. 1840
- [78] J. P. Chen, X. Wang, Removing copper, zinc, and lead 1841
ion by granular activated carbon in pretreated fixed- 1842
bed columns, *Sep. Purif. Technol.* 19 (2000) 157–167. 1843
doi:10.1016/S1383-5866(99)00069-6. 1844
- [79] K. Kadirvelu, C. Faur-Brasquet, P. L. Cloirec, Removal 1845
of Cu(II), Pb(II), and Ni(II) by adsorption onto acti- 1846
vated carbon cloths, *Langmuir* 16 (2000) 8404–8409. 1847
doi:10.1021/1a0004810. 1848
- [80] Y. Zhang, C. Liu, W. Shi, Z. Wang, L. Dai, X. Zhang, 1849
Direct measurements of the interaction between pyrene 1850
and graphite in aqueous media by single molecule 1851
force spectroscopy: Understanding the π - π interac- 1852
tions, *Langmuir* 23 (2007) 7911–7915. doi:10.1021/ 1853
1a700876d. 1854
- [81] C. Ehli, N. Jux, D. Balbinot, G. M. A. Rah- 1855
man, D. M. Guldi, F. Paolucci, M. Marcaccio, 1856
D. Paolucci, M. Melle-Franco, F. Zerbetto, S. Campi- 1857
delli, M. Prato, Interactions in Single Wall Carbon Nan- 1858
otubes/Pyrene/Porphyrin Nanohybrids, *J. Am. Chem. 1859*
Soc. 128 (2006) 11222–11231. doi:10.1021/ja0624974. 1860
- [82] T. L. Sordo, J. A. Sordo, R. Flórez, Theoretical study 1861
of adsorption of hydrocarbons on graphite, *J. Com- 1862*
put. Chem. 11 (1990) 291–296. doi:10.1002/jcc. 1863
540110303. 1864
- [83] J. T. Dickinson, J. J. Shin, S. C. Langford, The role 1865
of defects in laser induced positive ion emission from 1866
ionic crystals, *Appl. Surf. Sci.* 96–98 (1996) 316–320. 1867
doi:10.1016/0169-4332(95)00436-X. 1868
- [84] D. Duca, C. Irimiea, A. Faccinetto, J. A. Noble, M. Vo- 1869
jkovic, Y. Carpentier, I. K. Ortega, C. Pirim, C. Focsa, 1870
On the benefits of using multivariate analysis in mass 1871
spectrometric studies of combustion-generated aerosols, 1872
Faraday Discuss. 218 (2019) 115–137. doi:10.1039/ 1873
C8FD00238J. 1874
- [85] C. Focsa, D. Duca, J. A. Noble, M. Vojkovic, Y. Car- 1875
pentier, C. Pirim, C. Betrancourt, P. Desgroux, 1876
T. Trischer, J. Spielvogel, M. Rahman, A. Boies, 1877
K. F. Lee, A. N. Bhave, S. Legendre, O. Lancry, 1878
P. Kreutziger, M. Rieker, Multi-technique physico- 1879
chemical characterization of particles generated by a 1880
gasoline engine: towards measuring tailpipe emissions 1881
below 23 nm, *Atmos. Environ.* 235 (2020) 117642. doi: 1882
10.1016/j.atmosenv.2020.117642. 1883
- [86] P. A. Turhanen, J. J. Vepsäläinen, S. Peräniemi, Ad- 1884
vanced material and approach for metal ions removal 1885
from aqueous solutions, *Sci. Rep.* 5 (2015) 8992. doi: 1886
10.1038/srep08992. 1887
- [87] S. Cao, B. Li, R. Zhu, H. Pang, Design and synthe- 1888
sis of covalent organic frameworks towards energy and 1889
environment fields, *Chem. Eng. J.* 355 (2019) 602–623. 1890
doi:10.1016/j.cej.2018.08.184. 1891
- [88] D. Benetti, R. Nouar, R. Nechache, H. Pepin, 1892
A. Sarkissian, F. Rosei, J. MacLeod, Combined mag- 1893
netron sputtering and pulsed laser deposition of TiO_2 1894
and $BFCO$ thin films, *Sci. Rep.* 7 (2017) 2503–2512. 1895
doi:10.1038/s41598-017-02284-0. 1896
- [89] H. Matsumura, H. Umemoto, K. K. Gleason, 1897
R. Schropp, Catalytic Chemical Vapor Deposition: 1898
Technology and Applications of Cat-CVD, Wiley-VCH, 1899
Germany, 2019. 1900
- [90] J. Perrière, C. Hebert, N. Jedrecy, W. Seiler, O. Zanel- 1901
lato, X. Portier, R. Perez-Casero, E. Millon, M. Nis- 1902
tor, On the relevance of large scale pulsed-laser depo- 1903
sition: Evidence of structural heterogeneities in ZnO 1904
thin films, *J. Appl. Phys.* 116 (2014) 123502. doi: 1905
10.1063/1.4896379. 1906
- [91] F. Chiarella, C. A. Perroni, F. Chianese, M. Barra, 1907
G. M. De Luca, V. Cataudella, A. Cassinese, 1908
Post-Deposition Wetting and Instabilities in Organic 1909
Thin Films by Supersonic Molecular Beam Depo- 1910
sition, *Sci. Rep.* 8 (2018) 12015. doi:10.1038/ 1911
s41598-018-30567-7. 1912
- [92] C. Irimiea, A. Faccinetto, X. Mercier, I. K. Ortega, 1913
N. Nuns, E. Therssen, P. Desgroux, C. Focsa, Unveiling 1914
trends in soot nucleation and growth: When secondary 1915
ion mass spectrometry meets statistical analysis, *Car- 1916*
bon 144 (2019) 815–830. doi:10.1016/j.carbon.2018. 1917
12.015. 1918
- [93] C. Irimiea, A. Faccinetto, Y. Carpentier, I. K. Ortega, 1919
N. Nuns, E. Therssen, P. Desgroux, C. Focsa, A com- 1920
prehensive protocol for chemical analysis of flame 1921
combustion emissions by secondary ion mass spectrometry, 1922
Rapid Commun. Mass Spectrom. 32 (2018) 1015–1025. 1923

1859 doi:10.1002/rcm.8133.
1860 [94] J. Dunkley, M. Bucher, P. G. Ferreira, K. Moodley,
1861 C. Skordis, Fast and reliable Markov chain Monte Carlo
1862 technique for cosmological parameter estimation, *Mon.*
1863 *Not. R. Astron. Soc.* 356 (2005) 925–936. doi:10.1111/
1864 j.1365-2966.2004.08464.x.
1865 [95] J. Akeret, S. Seehars, A. Amara, A. Refregier, A. Csil-
1866 laghy, CosmoHammer: Cosmological parameter esti-
1867 mation with the MCMC Hammer, *Astron. Comput.* 2
1868 (2013) 27–39. doi:10.1016/j.ascom.2013.06.003.
1869 [96] D. Foreman-Mackey, D. W. Hogg, D. Lang, J. Good-
1870 man, EMCEE: The MCMC Hammer, *Publ. Astron.*
1871 *Soc. Pac.* 125 (2012) 306–312. doi:10.1086/670067.
1872 [97] S. T. Buckland, K. P. Burnham, N. H. Augustin, Model
1873 selection: an integral part of inference, *Biometrics* 53
1874 (1997) 603–618. doi:10.2307/2533961.
1875 [98] D. R. Anderson, “Chapter 5: Multimodel inference” in
1876 *Model based inference in the life sciences: A primer on*
1877 *evidence*, Springer Science & Business Media LLC, New
1878 York, 2007.